Reports on Progress in Physics

REVIEW

Punching holes in light: recent progress in single-shot coded-aperture optical imaging

To cite this article: Jinyang Liang 2020 *Rep. Prog. Phys.* **83** 116101

IOP Publishing Reports on Progress in Physics
Rep. Prog. Phys. **83** (2020) 116101 (32pp) https://doi.org/10.1088/1361-6633/abaf43

Review

Punching holes in light: recent progress in single-shot coded-aperture optical imaging

Jinyang Liang

Laboratory of Applied Computational Imaging, Centre Énergie Matériaux Télécommunications, Institut National de la Recherche Scientifique, 1650 boulevard Lionel-Boulet, Varennes, Québec J3X1S2, Canada

E-mail: jinyang.liang@emt.inrs.ca

Received 1 March 2020, revised 6 July 2020
Accepted for publication 13 August 2020
Published 27 October 2020

Abstract

Single-shot coded-aperture optical imaging physically captures a code-aperture-modulated optical signal in one exposure and then recovers the scene via computational image reconstruction. Recent years have witnessed dazzling advances in various modalities in this hybrid imaging scheme in concomitant technical improvement and widespread applications in physical, chemical and biological sciences. This review comprehensively surveys state-of-the-art single-shot coded-aperture optical imaging. Based on the detected photon tags, this field is divided into six categories: planar imaging, depth imaging, light-field imaging, temporal imaging, spectral imaging, and polarization imaging. In each category, we start with a general description of the available techniques and design principles, then provide two representative examples of active-encoding and passive-encoding approaches, with a particular emphasis on their methodology and applications as well as their advantages and challenges. Finally, we envision prospects for further technical advancement in this field.

Keywords: coded aperture, computational imaging, single-shot optical imaging, image reconstruction techniques, optical instrumentation

(Some figures may appear in colour only in the online journal)

1. Introduction

1.1. Advantages and limitations of single-shot optical imaging

Single-shot optical imaging has a wide range of applications and notable advantages in practical operation. By recording a scene with only one exposure, it can capture numerous dynamic events that are either non-repeatable or difficult to reproduce. Examples include laser-induced damage [1], irreversible chemical reactions [2], and neural signaling [3]. To record such events, multiple-shot techniques based on spatial and/or temporal scanning are inapplicable, and single-shot optical imaging proves indispensable to studying the underlying mechanisms [4]. From the perspective of practical operation, single-shot optical imaging is more robust and can produce more accurate results than its multiple-shot counterparts. Certain phenomena vary significantly over time or occur seldom. Examples include laser-driven implosion and dense plasma generation by high-energy, low-repetition laser systems [5–7]. For these cases, scanning-based multiple-shot methods would lead to significant inaccuracy and scant data with reduced utility. In contrast, single-shot optical imaging is more resilient to disturbances such as vibrational and other environmental noises [8] and can avoid artifacts created by the scanning units [9, 10].

Despite these clear merits, single-shot optical imaging presents many challenges. First, the single exposure often leads to a low signal-to-noise ratio (SNR) when there is a limited photon budget. This limitation is further aggravated when the maximum illumination intensity is constrained for safety

'Corresponding Editor Professor Masud Mansuripur'.

or if the objects have already been boosted to their saturation state [11]. In these scenarios, high brightness light sources contribute little to enhancing the image quality [12, 13]. Moreover, conventional single-shot optical imaging systems can measure the light intensity in only two dimensions (i.e. x and y), so much of the information carried by light is lost.

1.2. Introduction to using coded apertures in single-shot optical imaging

The limitations of conventional single-shot optical imaging can be overcome by implementing coded apertures in imaging systems. The coded aperture—in its original form, basically a mask containing many pinholes—was first devised to solve the inevitable trade-off between the spatial resolution and the light throughput in a single-pinhole camera [14]. With a coded aperture, element images produced by each individual pinhole were overlapped on a film that recorded them all simultaneously in a single exposure. The acquired data were then processed digitally to recover the image of the object. Although initially used with high-energy radiation (e.g. x-rays or gamma rays), the operating principle of coded-aperture imaging was later adopted for single-shot optical imaging as a novel sensing paradigm [15–19].

Single-shot coded-aperture optical imaging is a hybrid imaging scheme. In general, its operation can be divided into a physical data acquisition process followed by a computational image reconstruction process. In data acquisition, the incident light from a scene, I, is modulated by a coded aperture with various other hardware to produce the recorded data, E. This process can be expressed by a forward model of

$$E = \mathbf{O}I, \tag{1-1}$$

where $\mathbf{O}$ stands for the overall operation performed by the hardware. Different from conventional optical imaging, the acquired data often bears no apparent resemblance to the scene. Hence the image is computationally reconstructed to retrieve the image of the scene, $\hat{I}$, via a backward model of

$$\hat{I} = \mathbf{O}'E, \tag{1-2}$$

where $\mathbf{O}'$ stands for the inverse operation of $\mathbf{O}$ and is performed by the software.

1.3. Advantages of single-shot coded-aperture optical imaging

Although adding a coded aperture increases the system's complexity, it provides many attractive advantages over conventional counterparts. From the perspective of optical signal processing, coded apertures enable optically implementing various advanced mathematical models, including frequency multiplexing [20], compressed sensing [21], and phase-space computing [22]. Also, the prior information provided by a coded aperture assists in designing a specific inversion matrix to optimize image reconstruction [23]. Such a design can transfer many unique properties embedded in these mathematical models into the optical imaging systems. This valuable redefinition of imaging problems significantly expands the design space and enables compact yet high-performance imaging systems. In particular, a coded aperture permits simultaneously measuring information from different photon tags—variables that describe the photon's properties in space, directions, time, spectrum, and polarization [24–26]. Meanwhile, with thoughtful design of the coded aperture, the resulting system enjoys high light throughput and thus increases the SNR in data acquisition (referred to as the Jacquinot advantage) [27]. The superior quality of the measured data also can provide greater contrast in the reconstructed image (referred to as the Fellgett advantage) [28]. Capitalizing on these advantages, single-shot coded-aperture optical imaging has been an active research area, with new system designs and concepts constantly reported. Numerous studies advance the imaging speeds, fields of view (FOVs), resolutions, and measurement sensitivity of existing systems. These new and improved systems are quickly deployed to explore new applications across numerous disciplines, including biomedicine, physics, and materials science.

Single-shot coded-aperture optical imaging benefits further from the convenience of optical instrumentation and advances in digital reconstruction. Compared to high-energy radiation, light is much easier to modulate. Thus, coded apertures for optical imaging can be easily generated by using various manipulations of light (e.g. transmission, reflection, and refraction) in both the spatial and temporal domains. This flexibility has led to the development of numerous types of coded apertures for optics. Among them, a notable propelling force is the advent and implementation of spatial light modulators (SLMs). For example, electro-optic modulators have been employed as high-speed shutters for temporal encoding [29]. Micro-electromechanical-system-based digital micromirror devices (DMDs) [30] and liquid crystal SLMs [31, 32] have been widely used to produce high-resolution spatial encoding masks. Further, these programmable SLMs can be used to refine coded apertures based on measurement feedback. Compared with their fixed counterparts [33–36], programmable coded apertures enhance the performance and versatility of imaging systems.

From the perspective of digital reconstruction, the continuous improvement in computational power has enabled implementing sophisticated reconstruction frameworks for single-shot coded-aperture optical imaging. New generations of CPUs and graphics processing units provide ever-stronger hardware resources for reconstruction algorithms. Newly developed computational paradigms, such as parallel computing and machine learning, have significantly enhanced the speed and accuracy of image reconstruction. The superior performance of these algorithms, in turn, relaxes the constraints on the optical instrumentation [37]. In summary, the synergy between optical engineering, mathematics, and computer science has enabled single-shot coded-aperture optical imaging to flourish.

1.4. Scope of this review

Although the development of single-shot coded-aperture optical imaging is burgeoning, to our knowledge, there is no

timely and comprehensive survey of the field. Many reviews of coded-aperture imaging solely discuss its operation with high-energy radiation [27, 38]. Although the single-shot aspect is mentioned, recent advances in the optical regime are not covered. The desirability of such a review becomes even more apparent with the realization that discussions of single-shot coded-aperture optical imaging are often scattered among other disciplines in optics, including structured-light imaging, wavefront engineering, and lensless imaging. However, the mainstream of work in these fields concerns multiple-shot techniques, and how a coded aperture can allow single-shot acquisition is often only briefly mentioned. Furthermore, as a discipline in computational imaging, single-shot coded-aperture optical imaging has overlapped with other concepts, such as computational photography and computational cameras [39]. Nonetheless, computational photography techniques focus more on combining multiple images computationally for vision or graphic tasks. Work on computational cameras emphasizes modifying conventional consumer cameras to serve specific purposes. The major conceptual differences among these fields would benefit highly from distinction and individual scrutiny. Finally, researchers in optics and in computer science are often unaware of the latest developments in one another's fields. It is necessary to bridge this gap. All of these reasons call for an in-depth summary of the field that can benefit a broad readership from diverse communities.

In this review, we comprehensively survey the cutting-edge techniques in single-shot coded-aperture optical imaging and their associated applications. For clarification, we define key terms as follows. 'Single-shot' (also often refers to as 'snapshot' and 'one-shot') is defined as the capability of capturing all required information in a single acquisition. Adopting the definition from established literature [40], we limit the term 'coded-aperture' to refer to patterned masks that spatially and/or temporally modulate light intensity. However, extending the conventional definition, we do not restrict the location of the coded aperture in the system. 'Optical' refers to detecting photons in the spectral range from the extreme ultraviolet to the far infrared. Finally, 'imaging' takes place in at least two spatial dimensions, i.e. x, y. As a result, we do not discuss multiple-shot coded-aperture optical imaging methods, such as phase-shifting-based three-dimensional (3D) profilometry [41, 42], single-pixel imaging [43, 44], multi-encoding temporal imaging [45], hyperspectral imaging based on multiple coded apertures [46], variable-aperture-based light-field imaging [47], synthetic-aperture-based microscopy [48], and time-division imaging polarimetry [49]. We also exclude one-dimensional single-shot coded-aperture optical imaging [50]. Moreover, uniform modulation of the light intensity (e.g. intensity attenuation using a neutral density filter) and modulation of light properties without an intensity change (e.g. angular modulation of an incident beam using a mirror) are not considered as coded apertures in this context. Finally, coded-aperture imaging using non-optical sources is beyond the scope here [38]. Interested readers can refer to the selected references cited here and the extensive literature elsewhere.

1.5. Structure of this review

To avoid exhaustive enumeration, instead of compartmentalizing the existing techniques by applications, single-shot coded-aperture optical imaging is categorized according to the measured photon tags [24, 51, 52]. Illustrated in figure 1, there are six categories: planar imaging, depth imaging, light-field imaging, temporal imaging, spectral imaging, and polarization imaging. Depending on the location of the coded aperture, each category is further divided into active-encoding and passive-encoding approaches. One representative example is selected for each approach. Active encoding provides direct ways to manipulate the illumination incident onto the scene and thus can leverage existing standard imaging tools (e.g. microscopes and cameras) for data acquisition. However, it is in general sensitive to all sorts of non-ideality of the objects, including their color, absorption, and reflection/scattering non-isotropy. Passive encoding allows coded apertures to be compactly built into a detection module and hence is non-intrusive to the scene. In addition, it does not require specialized active illumination, making it well suited for imaging self-luminescent and color-selective scenes. Altogether, these examples cover 12 ways of implementing coded apertures to achieve single-shot optical imaging. The in-depth discussion of each category starts with a brief summary of existing research, followed by a description of the representative techniques that includes details of systems' operating principles, the functions of coded apertures, mathematical models of data acquisition and image reconstruction, and associated applications. In the last section, a summary and an outlook conclude this review.

2. Planar imaging

In the early development of planar optical imaging, coded apertures were less popular choices because light could be easily manipulated, and two-dimensional (2D) sensors (e.g. charge-coupled device (CCD) and complementary metal-oxide-semiconductor (CMOS) cameras) were available. However, more recent developments have exploited the novel properties of coded apertures to enable many new functions and applications for single-shot planar imaging. Notable technical advancements include the enhancement of depth of focus by analyzing changes in the diffraction patterns of coded apertures at various distances [53, 54], the increase of spatial resolutions by implementing Penrose pixels on a sensor [55], and the design of ultra-thin photograph systems by modeling light propagation [56]. These developments also enable new applications, such as seeing through scattering media [57], characterizing imaging systems' aberration [58], and discerning details in surveillance and sports images [59, 60].

2.1. Temporally encoded grayscale illumination (TEGI) microscopy

As a representative active-encoding approach, temporally encoded grayscale illumination (TEGI) microscopy [61] is used to remove motion blur in single-shot planar imaging. Shown in figure 2(a), this technique is built upon an inverted

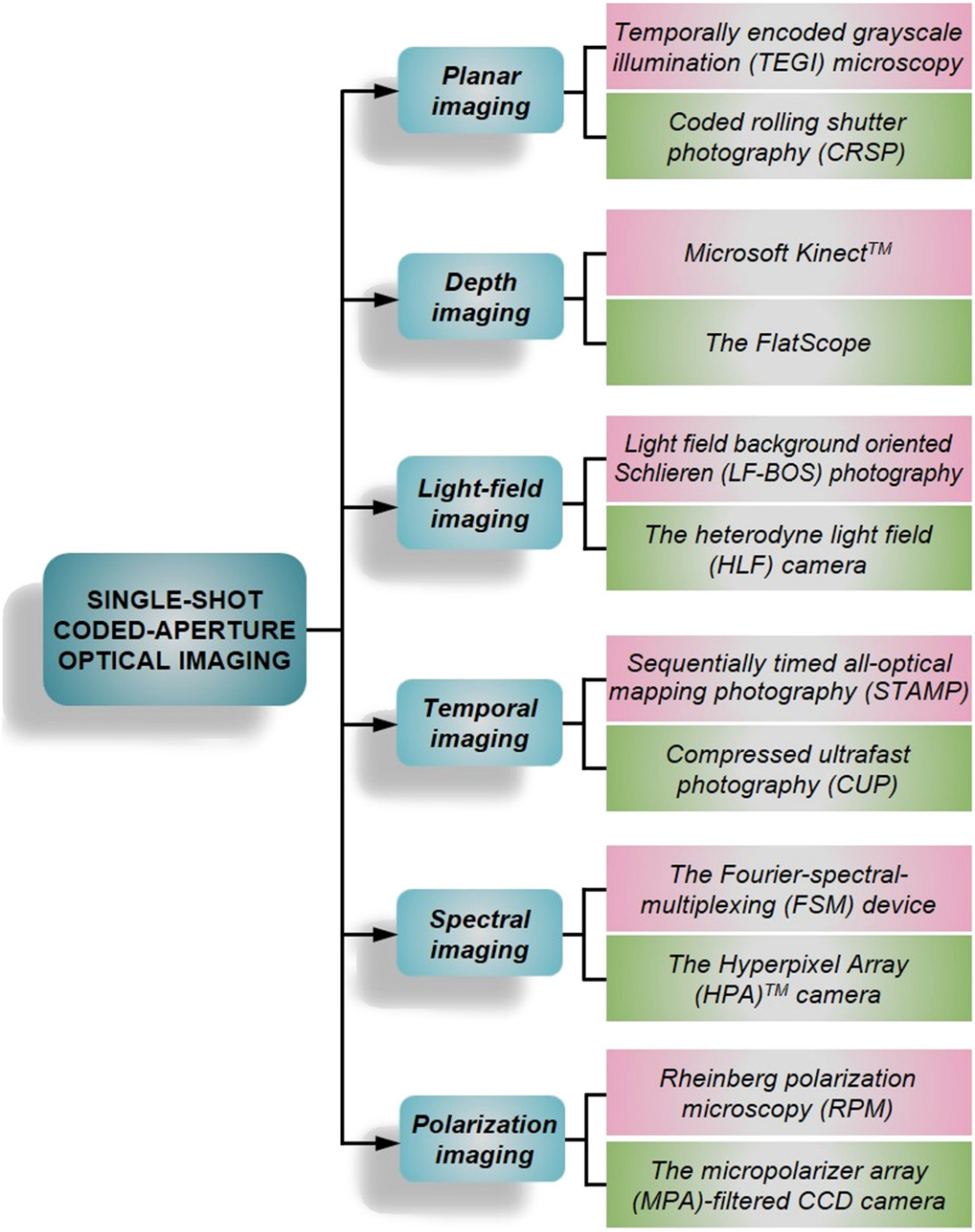

Figure 1. Categorization of single-shot coded-aperture optical imaging according to the measured photon tags. In each category, one active-encoding approach (magenta) and one passive-encoding approach (green) are detailed as representative techniques.

microscope with a custom-made light-emitting diode (LED) array at 70 mm above the sample. The LED array, capable of generating illumination with an 8-bit grayscale intensity, is synchronized with a scientific CMOS camera that is placed at the front port of the microscope. In data acquisition, the sample is moved on a motorized microscopy stage at a constant speed in one direction. The LED array displayed a temporally coded aperture with 30 time-steps, each of which lasts for 250 μs. The light intensity within each time-step is spatially uniform but with a different grayscale level. This coded illumination is captured by the camera with an exposure time of 10 ms.

The forward model of TEGI microscopy can be expressed using convolution. Neglecting noise, the acquired blurred image is expressed in matrix algebra by

$$E = AI + \eta. \tag{2-1}$$

Here η represents noise. A, denoted as the shearing matrix, describes the convolution of an input image with a point spread function (PSF) (figure 2(b)). Under the circumstance

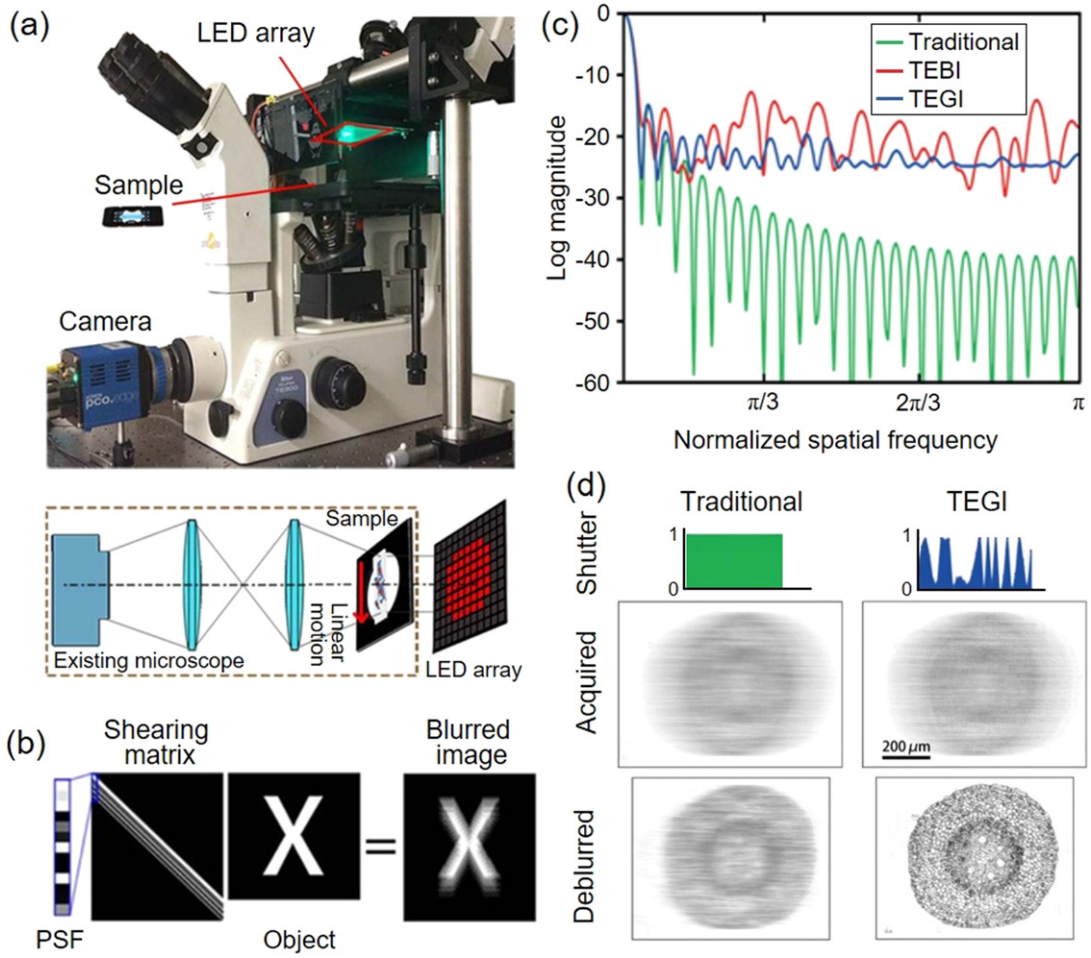

Figure 2. Temporally encoded grayscale illumination (TEGI) microscopy. (a) System setup. (b) Image formation of TEGI microscopy using matrix algebra. (c) Fourier spectra of traditional exposure, TEBI and TEGI. (d) Comparison of traditional exposure (left column) and TEGI (right column) in exposure schemes, acquired blurred images, and deblurred images. Adapted with permission from [61]. © OSA 2015.

of a one-direction motion blur, A is a circulant matrix. Its first column is the PSF vector of length of the time steps padded with $(N_r - 1)$ zeros, where N_r is the number of rows in the image. The next column is obtained from the previous one by circularly shifting the entries one step downward. This process continues until the PSF vector reaches the end of the column [62].

The matrix representation allows searching for the optimum temporally coded aperture, $T(t)$, with the best invertibility of the image reconstruction, by minimizing its condition number, i.e.

$$\min\ \kappa(A) \text{ subject to } \sum T(t) \geqslant \gamma \text{ and } 0 \leqslant T(t) \leqslant 1. \tag{2-2}$$

Here, $\kappa(A)$ denotes the condition number of A, and γ imposes a user-chosen threshold that balances the image quality, blur level, and light throughput. This non-convex optimization problem can be solved by nonlinear or intelligent optimization algorithms [61].

In image reconstruction, the captured image is digitally processed using a deconvolution model for motion deblurring:

$$\hat{I} = A'E, \tag{2-3}$$

where A' is the pseudo-inverse of A in the least-square sense. Figure 2(c) shows the frequency spectra of the traditional aperture (i.e. fully open during the exposure), the temporally encoded binary illumination (TEBI) [62], and the TEGI. The *sinc* function produced by the traditional aperture has large attenuation in most frequency ranges. Therefore, the deconvolution process is sensitive to noise, especially at the significantly attenuated frequencies, which is manifested by a large conditional number of 231. In comparison, the TEBI and TEGI methods have much lower conditional numbers of 17.3 and 12.9, respectively. Between the two temporal encoding patterns, TEGI is superior, demonstrating a flatter broadband response.

The motion deblurring ability of TEGI microscopy was demonstrated by imaging moving microscopic objects [61, 63]. As an example, figure 2(d) compares the results of using the traditional exposure and TEGI for imaging a moving *Zea mays* (maize) root cross section sample. The acquired raw data had similar levels of motion blurring. The blurred image generated by the traditional exposure was deblurred using the Richardson–Lucy algorithm [64, 65], which failed to recover the fine details. In contrast, the image acquired by the TEGI method was deblurred using the model in equation (2-3). TEGI

microscopy shows successful restoration of all spatial details in the deblurred image.

TEGI offers attractive advantages over previous attempts at motion deblurring. First, it allows motion deblurring without severely sacrificing light throughput. Conventional stroboscopic photography uses short flashes to freeze the motion [66], which, however, often leads to a low SNR and hence high noise in the image. In contrast, TEGI consists of many short flashes with carefully chosen intensity and time points, which largely enhances the overall light throughout. Since the advent of temporally coded exposure, numerous works have sought to better understand the underlying mathematical theory [67], to improve the technique's speed and accuracy [68], and to extend its application to spatially varying blurring [69]. With faster and brighter stroboscopic light sources, the motion deblurring ability could be further extended to fast and arbitrarily moving objects [62].

From the perspective of image reconstruction, TEGI provides a new method for accurate deconvolution. Numerous deconvolution methods, such as Wiener filtering [70], blind deconvolution [71], and iterative restoration [72], have been implemented to reduce image blurring by estimating PSFs, which, however, remains a challenging problem for arbitrary motions. Even with a known PSF, deblurred results have amplified noise from small terms, resulting in an unacceptably noisy reconstruction and resampling/quantization problems. High frequencies are usually lost in the deblurred results, and deblurring is often limited to blur from small movements [62]. TEGI, on the contrary, modulates the integration of motion in such a way that the resultant PSF has maximum coverage in the spatial frequency domain. This temporally coded aperture thus preserves high spatial frequencies and hence turns the corresponding deblurring into a well-posed problem. As a result, TEGI can accurately handle a large degree of motion blur with a relatively simple decoding process.

2.2. Coded rolling shutter photography (CRSP)

Coded rolling shutter photography (CRSP) [73] is a representative of passive encoding in single-shot coded-aperture planar imaging. Built upon CMOS image sensors (figure 3(a)), CRSP uses new logic in the address generators to control the desired row-reset (RST) and row-select (SEL) signals for coded readout and exposure. In a particular example, the pixel array of the CMOS image sensor is coded with staggered readout and three exposures—Δt_{e1}, Δt_{e2}, and Δt_{e3} (figure 3(b)). The readout timings of each row do not overlap, which still satisfies the requirement of CMOS architecture. Nevertheless, the single snapshot acquired by CRSP consists of three interlaced sub-frames with different exposure times (denoted as E_{e1}, E_{e2}, and E_{e3}).

In image reconstruction, the three sub-frames are extracted from the captured single snapshot (figure 3(c)) and are then resized vertically to full resolution using cubic interpolation. Next, E_{e1} and E_{e2} are used to calculate the camera motion and to estimate the blurring PSFs in the sub-frames. After motion compensation, two composed images, $E_{a1} = E_{e1} + E_{e2}$ and $E_{a2} = E_{e1} + E_{e2} + E_{e3}$ are computed for subsequent processing. These two composed images combine two or three down-sampled images at different phases (e.g. the image of all odd rows and the image of all even rows). Thus, this method effectively suppresses aliasing artifacts from interpolation [74]. With knowledge of motion and exposure times, E_{a1} and E_{a2} are deblurred by an optical flow algorithm [75]. The two deblurred images are denoted as E_{b1} and E_{b2}. Finally, the output image is computed by

$$\hat{I}_r = \frac{1}{3}\left(\frac{E_{e1}}{\Delta t_{e1}} + \frac{E_{b1}}{\Delta t_{e1} + \Delta t_{e2}} + \frac{E_{b2}}{\Delta t_{e1} + \Delta t_{e2} + \Delta t_{e3}}\right). \tag{2-4}$$

CRSP produced images with a high dynamic range and without motion blur. In the reported experiment, $\Delta t_{e3} = 4\Delta t_{e2} = 8\Delta t_{e1}$. Thus, the improvement in dynamic range was $20\log(\Delta t_{e3}/\Delta t_{e1}) = 18.06$ dB. A reconstructed image is shown in figure 3(d). Three zoomed-in views (marked by the red, green, and blue boxes) highlight the comparison among the three sub-frames (i.e. E_{e1}, E_{e2} and E_{e3}) and $\hat{I}_r$. With short exposures, the sub-frames (i.e. E_{e1} and E_{e2}) are dark and noisy. With a long exposure, E_{e3} is blurry and washed out. In comparison, only $\hat{I}_r$ has high contrast without motion blurring.

The technical advances of CRSP are manifested in three aspects. First, by controlling the readout timing and exposure length for each row of the CMOS sensor, the staggered readout of CRSP in data acquisition allows developing new image reconstruction methods to achieve a high dynamic range without motion blur. However, these new functions trade off the vertical resolution, which motivates future research on designing new encoding schemes that leverage existing de-interlacing methods [76–78] to increase vertical resolution. Second, single-shot data acquisition in CRSP avoids multiple-shot drawbacks—such as ghosting [79] and motion blur [80]—due to camera shake. These features make CRSP an attractive candidate for hand-held cameras and cell phones. Finally, CRSP is built upon existing architectures of CMOS sensors [81, 82]. The control of row-wise readout and exposure requires only implementing different logics in the address generator, without any expensive hardware redesigning [83]. Overall, the flexible and versatile controls offered by CRSP enhance CMOS sensors' performance for specific studies.

3. Depth imaging

Single-shot coded-aperture depth imaging is attracting research interest because of demands from widespread applications, such as on-line industrial inspection [84], multimedia [85], biomedicine [86], human-computer interaction [87], and security [8]. Among various approaches, structured-light profilometry, time-of-flight (ToF) light radar (LIDAR), light-field transportation are popular. In active-encoding approaches, coded apertures have been implemented temporally by sinusoidal intensity modulation of illumination in ToF–LIDAR [88], which extracts 3D surface information by detecting the phase shift in the backscattered signal [89]. Coded apertures have also been implemented spatially by structured light [90], which senses the depth of a surface by estimating the disparity

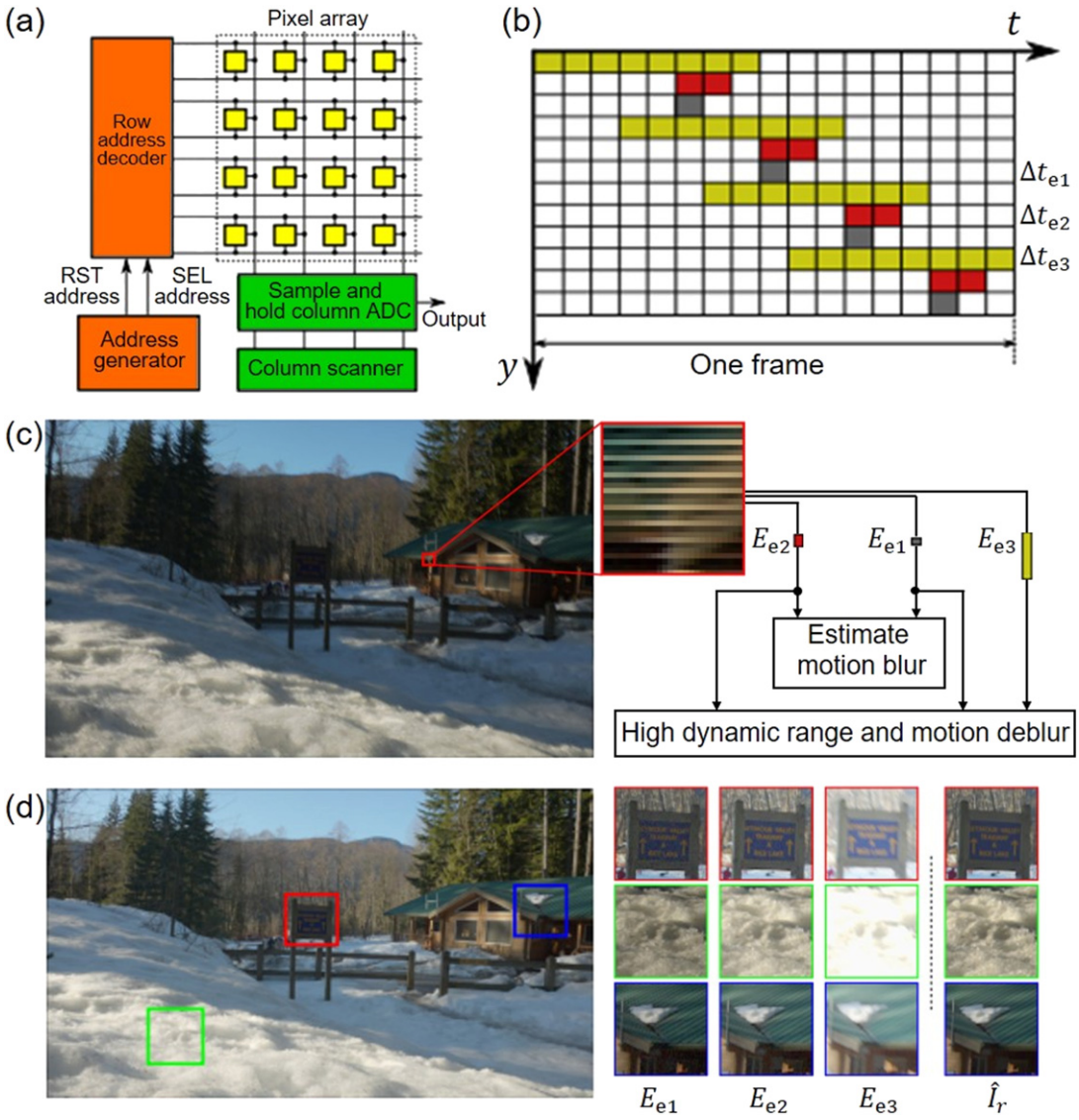

Figure 3. Coded rolling shutter photography (CRSP). (a) Architecture of a CMOS sensor. ADC, analog-to-digital converter; RST, Row-reset; SEL, Row-select. (b) Time sequence of staggered readout. (c) CRSP snapshot. The zoomed-in view shows the intensity difference in adjacent rows due to different exposure times. The flow chart on the right shows how the three sub-images are used to achieve high dynamic range and motion deblurring. (d) Reconstructed image of (c) (left image) and demonstration of high dynamic range (right images) in three selected regions (marked by the red, green, and blue boxes). © 2010 IEEE. Adapted with permission, from [73].

resulting from the deformation of the projected light pattern [91, 92]. Other commonly used methods in structured-light profilometry include color-encoded projection [93–95], grayscale indexing [96–101], and wrapped phase demodulation [102–105]. In passive-encoding approaches, most techniques use a depth-dependent PSF to indicate the image depth [106–111]. Typically, implementation involves placing a spatially encoded aperture between the camera lens and the sensor to estimate the depth by examining the shape transformation of the aperture over depth [112]. Frequency analysis, extended from planar imaging (section 2.1), is used to optimize coded apertures for producing a more reliable and precise depth map from defocusing than can be achieved with traditional circular apertures [113–115]. Besides the efforts in design optimization, polarization and color have been used to multiplex measurements [116, 117]. These methods can separate information mixed in the single acquisition in a reciprocal domain, which is then used to recover the depth information.

3.1. Microsoft Kinect™

Microsoft Kinect™ for Xbox 360, a representative active-encoding approach to single-shot code-aperture depth imaging [118, 119], uses structured light to capture depth information. As shown in figure 4(a), an 825 nm infrared projector illuminates a 3D (x, y, z) scene with a dot-array pattern. The scattered photons are captured by an infrared camera. In addition, a visible light camera between the infrared projector and the infrared camera captures color images.

Before data acquisition, the Kinect™ device is calibrated off-line by using a highly reflective surface at a known distance z_{REF} [120]. The captured image, denoted as E_{REF} (see the first

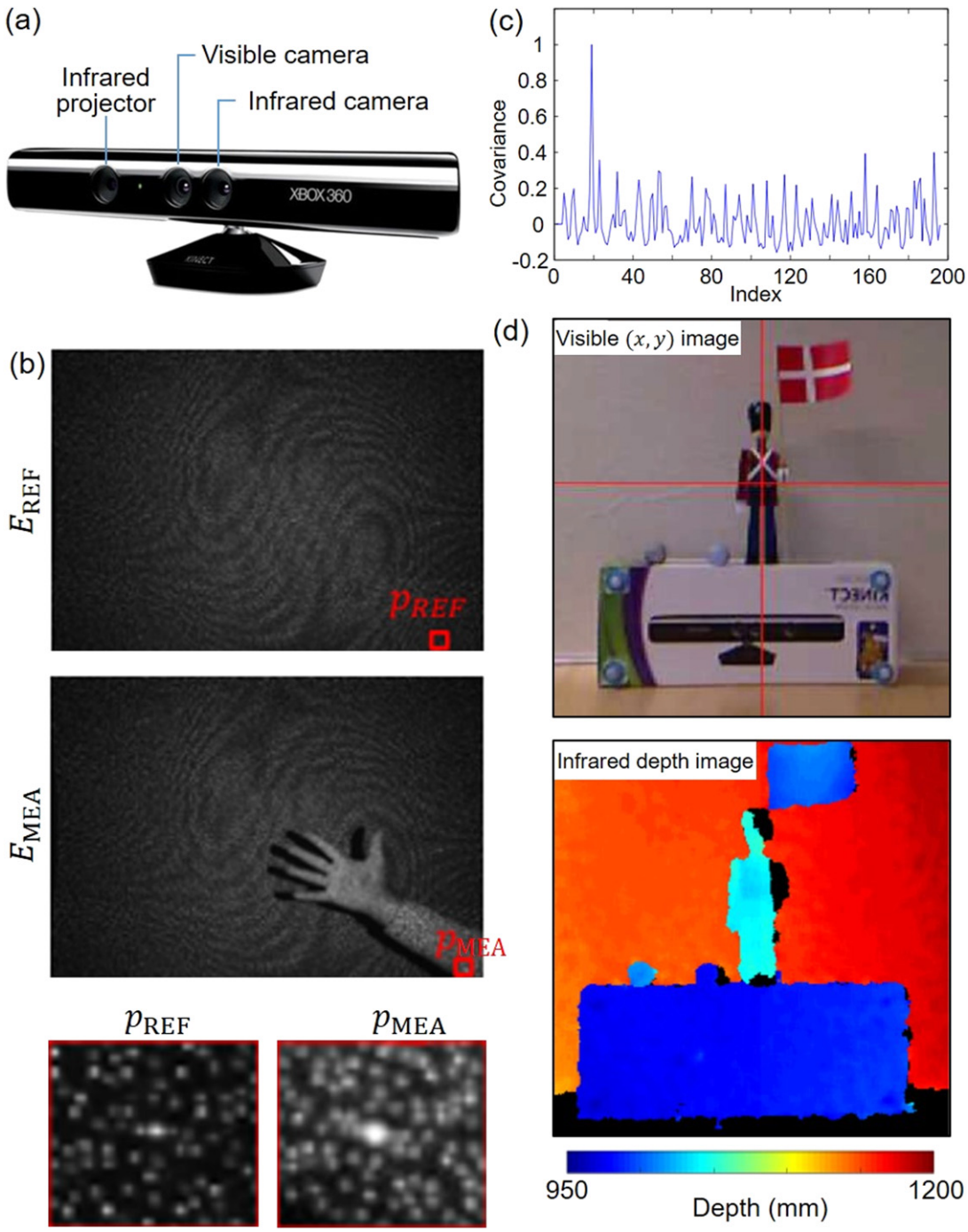

Figure 4. Microsoft Kinect™ for Xbox 360. (a) Structure of the device. (b) Projected coded pattern on a flat surface for reference image acquisition (first row) and on a 3D surface for actual measurement (second row). Third row: comparison of a codeword (marked by the red solid boxes in images in the first and the second rows). (d) Covariance of a measured codeword with its corresponding pair. (d) Visible image (top) and depth image (bottom) generated by the Kinect™ device. (a)–(c) Adapted by permission from Springer Nature Customer Service Centre GmbH: Springer [119] © 2012. (d) Adapted from [118]. CC BY 3.0.

row in figure 4(b)), records the dot-array patterns. This calibration process compensates for all the non-idealities in both the projector and the cameras, such as illumination non-uniformity and image distortion. In data acquisition, a single image of the dot-array pattern distorted by an unknown 3D surface is recorded, denoted as E_{MEA} (see the second row in figure 4(b)).

In image reconstruction, the first step of depth calculation is to find the relative disparity, d_{REL}, of each pixel over the entire FOV between E_{MEA} and E_{REF}. In particular, a codeword is defined for each pixel. This codeword contains a square array of pixels, with the targeted pixel in the center (see the third row in figure 4(b)). In this case, neighboring pixels share parts of their codewords, thus making their coding interdependent. To balance the accuracy of calculation and the interdependence of codewords, windows of 7×7 [121] or 9×9 [122] pixels have typically been chosen as the size for a codeword. An algorithm calculates the local similarity in covariance between all the pairs of possible conjugate points and selects the pair

that maximizes it. For example, figure 4(c) shows the covariance of a codeword of a 9 × 9 pixel window centered at the coordinates (19, 5) with the corresponding potential pair of the same row. It peaks at $n_x = 19$, indicating no lateral disparity for this pixel. The second step is to refine the computed disparity map. The values returned from the covariance calculation are integers, which limit depth resolution [123, 124]. This limitation can be offset by a sub-pixel refinement technique with an interpolation ratio of eight [121]. The last step in image reconstruction is to compute the depth map using triangulation. Given the known distance between the projector and the camera (denoted by b) and the focal length of the camera and the projector (denoted by f), the measured depth, z_{MEA} , can be calculated by

$$z_{\mathrm{MEA}} = \frac{bf z_{\mathrm{REF}}}{d_{\mathrm{REL}} z_{\mathrm{REF}} + bf}. \tag{3-1}$$

Figure 4(d) illustrates an example of a visible image and its depth map captured by the Kinect™ device [118]. The black pixels in the depth image reflect areas of unknown depth, which in this example are due to the noise and shadow effect on the left side. The image is 640 × 480 pixels, with a depth range from 0.5 to 15 m and with an imaging speed of 30 frames per second (fps) [119]. Besides being the most popular application in the gaming industry, the Kinect™ device has been used in numerous scientific studies that involve human-computer interaction [125]. For example, it allows using hand and arm gestures for interactive exploration of medical images [126], and its touch-free interface makes it suitable for use in operating rooms. Other applications of Kinect™ include robotics [127], metrology [128], and augmented reality [129].

Microsoft Kinect™ for Xbox 360 uses a randomly distributed dot pattern as a coded aperture. The random distribution of the dots enables identifying interdependent local codewords for computing the depth information. This grid-index matching based method is easy to implement, well suited for capturing dynamic scenes, and capable of dealing with occlusions. However, it presents operational challenges, including low imaging contrast in the presence of high intensity of wide-spectrum ambient light [130] and potential interference between multiple sensors used simultaneously [131–133].

3.2. The FlatScope

The FlatScope is a representative of the passive-encoding-based techniques in single-shot coded-aperture depth imaging [134, 135]. Shown in figures 5(a) and (b), the FlatScope—the world's tiniest and lightest microscope—is constructed by adding a binary transmissive coded aperture, termed a modified uniformly redundant array (MURA) pattern (detailed in the next paragraph), ∼0.2 mm in front of a CMOS sensor. The coded aperture is fabricated by photo-lithographically patterning a 100 nm-thick film of chromium that is deposited onto a 170 μm-thick fused silica glass wafer. The MURA coded aperture has a minimum feature size of 3 μm. Under a microscope, the coded aperture is aligned with the pixels of the imaging sensor. To filter blue light, an absorptive filter is epoxied to the coded aperture. Finally, the device is conformally coated with a <1 μm-thick parylene layer for insulation. The resultant FlatScope, a lensless microscope, is scarcely larger than an image sensor (∼0.2 g in weight and <1 mm in thickness).

In data acquisition, the scene is encoded by the MURA coded aperture, denoted by M. Given a prime number p of the form $p = 4w + 1$ (w is an integer), MURA is of size $p \times p$. Let $i = 0, \ldots, p-1$ and $j = 0, \ldots, p-1$ index the rows and the columns, and then the MURA pattern can be written as [136]

$$M_{ij} = \begin{cases} 0, & \text{if } i = 0 \\ 1, & \text{if } j = 0,\ i \neq 0 \\ 1, & \text{if } C_i C_j = 1 \\ 0, & \text{if } C_i C_j = -1 \end{cases}, \tag{3-2}$$

where

$$C_i \text{ and } C_j = \begin{cases} 1, & \text{if } i \text{ or } j \text{ is a quadratic residue modulo } p \\ -1, & \text{otherwise} \end{cases}. \tag{3-3}$$

A MURA coded aperture, akin to previous URA patterns, possesses many attractive advantages [136]. It can produce a high SNR in measurement. Moreover, its autocorrelation is a δ function. Furthermore, an MURA can be designed as a square pattern, which is more easily adapted to the sensors. Finally, the symmetric nature of an MURA can assist in developing new and faster decoding algorithms.

The FlatScope leverages the separability property of an MURA in its data acquisition. To prove this property, the first row (i.e. $i = 0$) and the first column (i.e. $j = 0$) of the original MURA are dropped. The remaining pattern, with a size of $(p-1) \times (p-1)$, can be defined as

$$M_{ij} = \begin{cases} 1, & \text{if } C_i C_j = 1 \\ 0, & \text{if } C_i C_j = -1 \end{cases}. \tag{3-4}$$

With the definition of $C_I = C_J = \{C_i\}_{i=1}^{p}$, M can then be written in the separable form of

$$M = \frac{1 + C_I C_J^T}{2}. \tag{3-5}$$

The separable coded aperture allows the local spatially varying PSF to be decomposed into two independent terms [135]. Given a 3D (x, y, z) scene I that is discretized into a superposition of planar samples I_d at D different depths, the FlatScope captures it into a 2D (x, y) snapshot by

$$E = \sum_{d=1}^{D} \left(P_{\mathrm{o}d} I_d Q_{\mathrm{o}d}^T + P_{\mathrm{c}d} I_d Q_{\mathrm{c}d}^T \right). \tag{3-6}$$

Here P_{od} and P_{cd} operate only on the rows of I_d, and Q_{od} and Q_{cd} operate only on the columns of I_d (the subscripts 'o' and 'c' refer to 'open' and 'coding', respectively). The first term models the effect of a hypothetical 'open' mask (i.e. with no coded aperture), and the second term models the effect of the coding of the mask pattern.

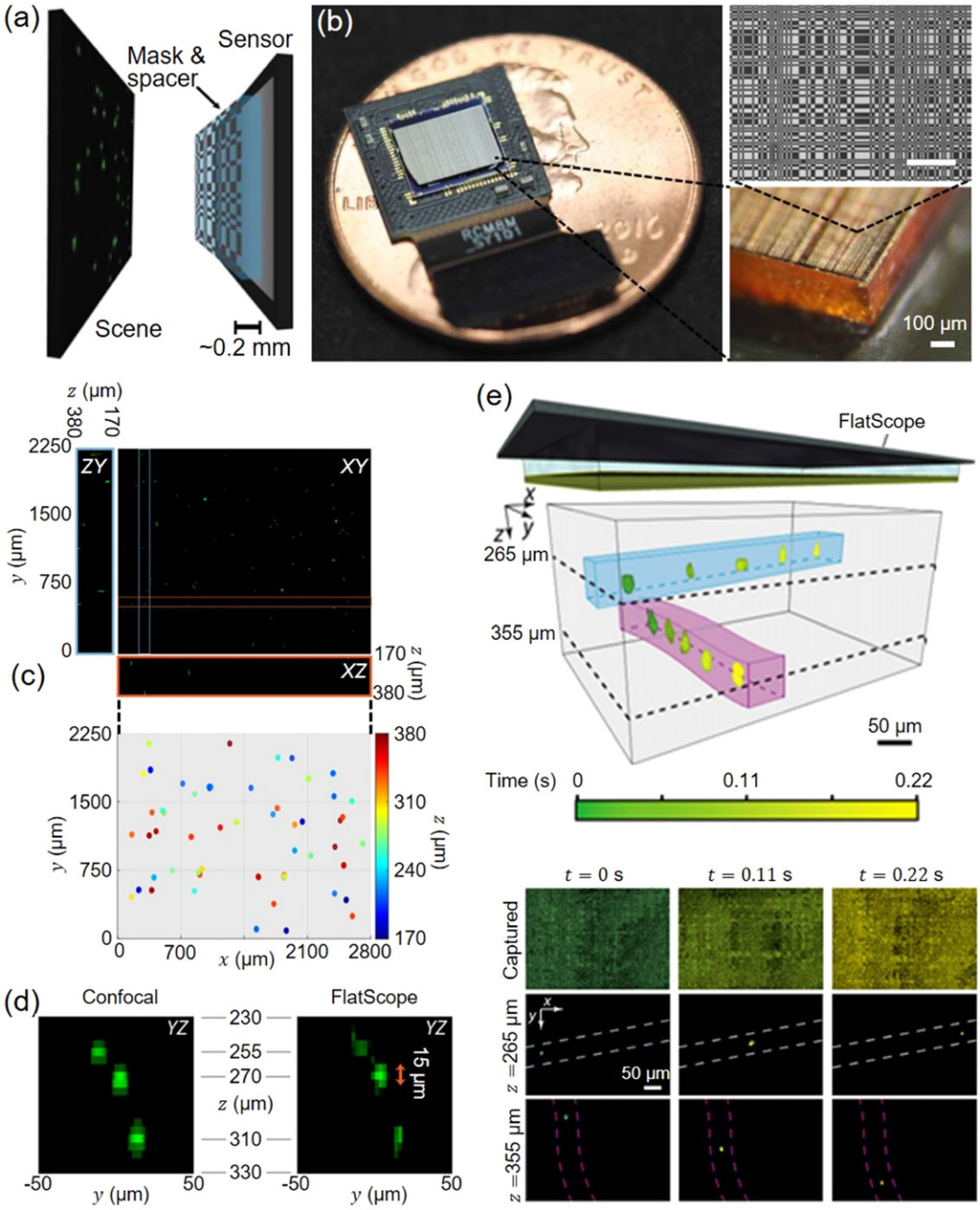

Figure 5. FlatScope. (a) Schematic of 3D fluorescence imaging using the FlatScope. (b) FlatScope prototype (left) with a zoomed-in view of the MURA coded aperture (top right) as well as the mask and spacer (bottom right). (c) 3D volume reconstruction of 10 μm fluorescent beads suspended in agarose. (d) Comparison of lateral and axial resolutions between confocal microscopy and FlatScope. (e) Top row: schematic of dynamic 3D fluorescence imaging using FlatScope. Bottom rows: representative captured frames and the corresponding reconstructed results for two different depths at three time points. From [135]. Reprinted with permission from AAAS.

A calibration procedure is executed to determine $\{P_{od}, P_{cd}\, Q_{od}, Q_{cd}\}$ for $d = 1, 2, \ldots, D$. A 5 μm slit is placed $\sim$10 cm in front of an LED array. To mimic an isotropic source and mitigate diffraction effects, a wide-angle diffuser is placed between the light source and the slit. In this way, the horizontal and vertical slits are translated over the FOV of the FlatScope over each depth plane d. For each measurement, a truncated singular value decomposition is used to estimate the columns of P_{od}, Q_{od}, P_{cd}, and Q_{cd}. This calibration needs to be performed only once, and the calibrated matrices stay valid as long as the coded aperture and sensor retain their relative positions.

In image reconstruction, the scene is recovered by using regularized least-square minimization. In particular, the 3D reconstruction problem was solved as a Lasso problem by

$$\hat{I} = \arg\min_{I} \left(\sum_{d=1}^{D} \| P_{od} I_d Q_{od}^T + P_{cd} I_d Q_{cd}^T - E \|_2^2 \right) + \lambda_1 \| I \|_1, \tag{3-7}$$

where $\|\cdot\|_2$ and $\|\cdot\|_1$ denote the l_2 and l_1 norms, respectively, and λ_1 is a weighting constant that balances the ratio between the two terms. In practice, equation (3-7) is solved by using the fast iterative shrinkage/thresholding algorithm [137]. The reconstruction converges to a solution in under 15 min. The reconstructed volumetric image had a lateral resolution of <2 μm, a depth resolution of <15 μm, and an FOV of 6.52 mm^2. Being lens-free, the FlatScope is not bounded by the fundamental trade-off between FOV and resolution. Consequently, for a given sensor size, the FlatScope can achieve a $10\times$ greater FOV than a traditional objective-lens-based microscope.

The FlatScope's imaging capability was first tested using 10 μm fluorescent beads suspended in an agarose solution. A single exposure of 30 ms was made. The top images of figure 5(c) show a FlatScope reconstruction as a maximum intensity projection along the x, y, and z axes. The bottom image of figure 5(c) shows the 3D positions of beads as estimated by the FlatScope. This result was verified by imaging the 3D fluorescent volume with a scanning confocal microscope as the ground truth. The acquisition of this ground truth required a total of 41 z-sections and took more than 20 min. The comparison shows that the FlatScope has sufficient resolution in both lateral and axial directions to resolve 3D fluorescent objects (figure 5(d)), and the single-shot volumetric imaging makes the FlatScope 40 000 times faster in data acquisition.

The FlatScope can capture 3D volumetric video at the native frame rate of the image sensor. This capability was demonstrated by imaging fluorescent beads flowing in two channels separated axially by $\sim$100 μm (see the upper image of figure 5(e)). The FlatScope was operated to capture 18 volumes per second. The images in the second to the fourth rows in figure 5(e) show the captured data and the reconstructed frames at $z = 265$ μm and at $z = 355$ μm at three representative time points.

The FlatScope can image complete 3D volumes of several cubic millimeters with a micrometer resolution at video rate. The implemented MURA coded aperture modulates the incoherent PSF, which makes high-frequency spatial information recoverable at various depths. The separable nature of this coded aperture (illustrated by equation (3-5)) massively reduces the number of images required for calibration. This feature, along with the amplitude modulation of the coded aperture, reduces the complexity of the reconstruction algorithm so that the image can be recovered from the sensor measurements in near real time. This new flat fluorescence microscopy paradigm may open new possibilities for implantable endoscopes that minimize tissue damage, arrays of imagers that cover large areas, and flexible microscopes that conform to complex topographies [135].

4. Light-field imaging

Light-field imaging records the amount of light from every direction that arrives at each point in the FOV [138]. Because light-field cameras are one of the most popular applications in this field, the single-shot requirement has guided the development of light-field imaging [139]. Coded apertures have been a popular choice in light-field imaging. In active-encoding approaches, coded apertures are used to engineer specifically designed illumination that maps a four-dimensional (4D) light field into intensity and color [140]. In addition, to achieve high spatial and angular resolutions, 4D light-field-encoded illumination can be implemented in holograms or dynamic parallax barrier displays [141]. Other techniques include using a 2D patterned pinhole array with ptychography [142] and tomography [143]. In passive-encoding approaches, system designs often leverage light-field modulation in the phase-space domain, including filtering by a photomask [144], convolution by a diffuser [145], shearing by light propagation [146], and distortion by a phase plate [147]. These developments have allowed recovering high-resolution light fields in lens-free and compact system architectures.

4.1. Light field background oriented Schlieren (LF-BOS) photography

Light field background oriented Schlieren (LF-BOS) photography is a representative of active-encoding approaches to single-shot coded-aperture light-field imaging [148, 149]. The system, shown in figure 6(a), consists of a light-field illumination module and a camera. The module is placed behind a refractive object and photographed by the camera.

The light-field illumination module (figure 6(b)) is composed of an LED lightbox, two stacked transparencies, and a lenslet array. The LED lightbox maintains consistent lighting throughout the capture process. Light-field codes are printed onto the transparencies underneath the lens array at a resolution of $\sim$57 dots per millimeter (i.e. 1440 dots per inch). For the first transparency, a green color gradient pattern is printed, which encodes the emitted light ray's location on the illumination module. For the second transparency, a periodic pattern of a red color gradient is printed to encode the emitted light's directions. A lenslet array (with a focal length of 3 mm (i.e. 0.12 inches) and a diameter of 2.29 mm (i.e. 0.09 inches)) is mounted at its focal distance from this color-coded background. Overall, this light-field illumination module produces smoothly modulated color and intensity that can be transferred to an angular resolution of 0.32°.

The design of this light-field illumination module enhances the system's robustness. The module and the camera are much further apart than the module and the refractive object. This arrangement yields a good approximation of a pinhole camera, which simplifies the model in light-field computation. Nevertheless, finite pixel sizes and small apertures, along with strong distortions of the wavefront caused by refraction, often amplify the integration area of each camera pixel in the space of the light-field illumination module. However, because of the smoothly modulated intensity and color produced by this light-field illumination module, even if the pinhole assumption breaks down and the captured colors degrade, the system can still acquire information about the 4D light field.

Before data acquisition, the system is calibrated to correct for the color transformations among specified digital images, the printer's gamut, and the color gamut of the camera. The colors of the pattern are defined by the device-specific CMYK

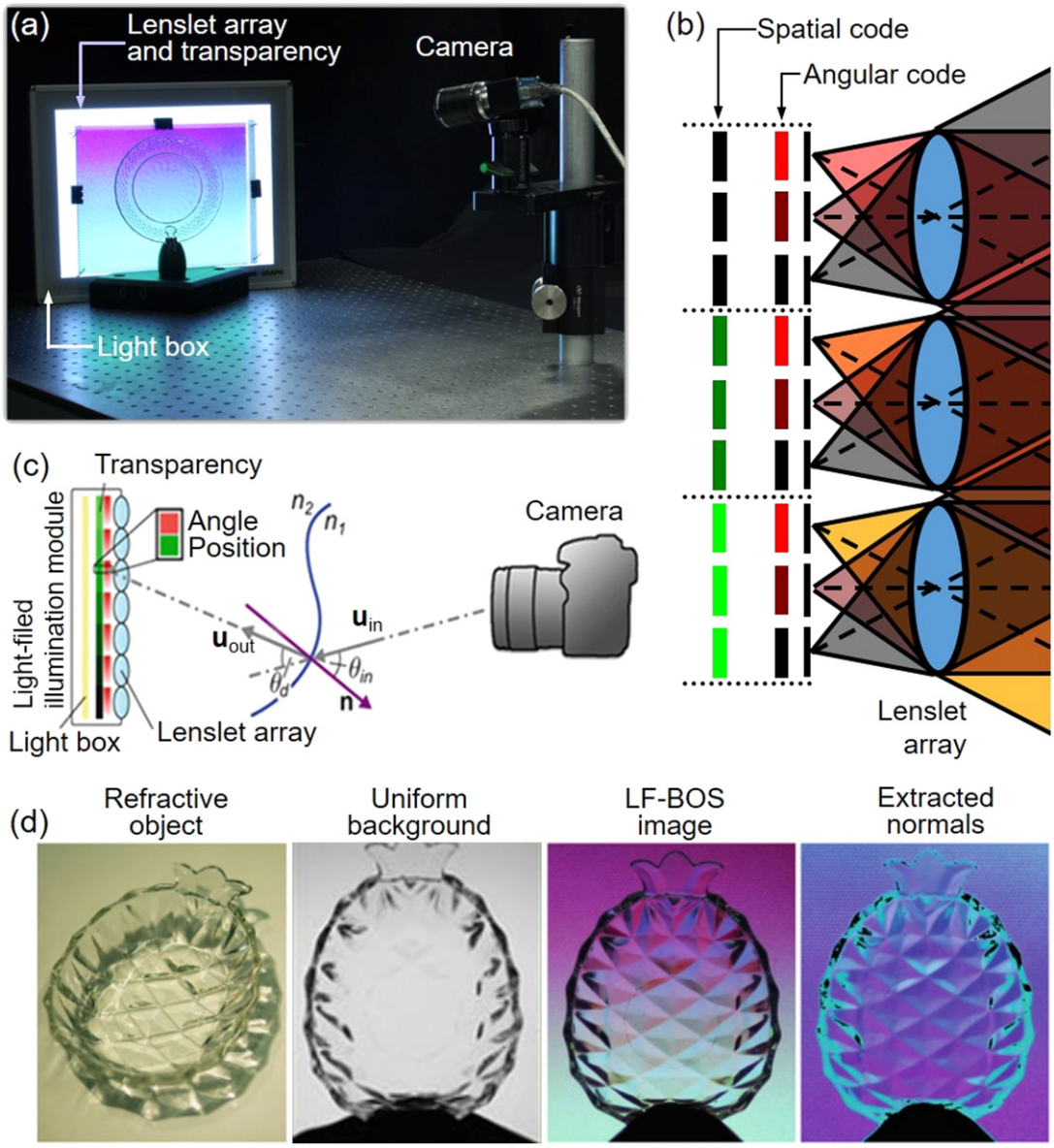

Figure 6. Light field background oriented Schlieren (LF-BOS) photography. (a) Prototype. (b) Design of the light-field illumination module. (c) Schematic showing the identification of position and its normal for each point on a surface of a transparent object. (d) LF-BOS photography of a transparent object. (a), (c) © 2011 IEEE. Adapted with permission, from [149]. (b), (d) Adapted by permission from Springer Nature Customer Service Centre GmbH: Springer [148] © 2014.

color gamut of the employed printer. Then they are printed with the device's internal color mappings disabled. Finally, the image of the light-field illumination module is recorded by the camera in sRGB space. In this way, captured photographs can be transferred into any desired color space as a post-processing step.

The refraction in the FOV is analyzed by tracing the surface normal of each point using Snell's law (figure 6(c)). The camera calibration provides the information of the incident normalized rays, denoted by $\boldsymbol{u}_{\text{in}}$. The refracted ray directions, $\boldsymbol{u}_{\text{out}}$, are also extracted from the imaged color. Thus, the total angle of difference, θ_{d}, is computed by $\theta_{\text{d}} = \cos^{-1}(\boldsymbol{u}_{\text{in}} \cdot \boldsymbol{u}_{\text{out}})$. For two media with known refractive indices (denoted by n_1 and n_2), the angle between an incoming ray and the surface normal is then given by

$$\theta_{\text{in}} = \tan^{-1}\left(\frac{n_2 \sin \theta_{\text{d}}}{n_2 \cos \theta_{\text{d}} - n_1}\right). \tag{4-1}$$

In this way, the surface normals are computed independently point by point.

Figure 6(d) shows reconstructions of a transparent solid glass object with a pineapple pattern, taken from a single shot. The front side of this object was flat and parallel to the fine details on the other side. The object was sufficiently thin that ray displacements within the glass were negligible. Under uniform background illumination, the central part could not be resolved. In contrast, the image captured by LF-BOS clearly shows this part as a flat triangle mesh.

In summary, LF-BOS photography uses a coded-aperture light-field illumination module to maps the directions of

emitted rays to color and intensity. This knowledge guides the light-field image reconstruction. Compared with previous Schlieren imaging techniques [150], LF-BOS photography has a more compact setup, can better handle strong refraction, allows separating objects and background during focus mismatch, and permits single-shot analysis. These advantages make it particularly well suited to imaging dynamic transparent events, such as water surfaces, gas movements, and liquid mixing. They also hold promise for the future development of cell-phone-based LF-BOS microscopy [151] to map scattering distribution functions. LF-BOS has two main limitations. First, the size of the refractive volume is limited by the size of the light-field illumination module. In addition, the implementation of the lenslet array trades angular resolution for spatial resolution. Alternative technologies, such as holographic light-field encoding [152], could achieve high spatial and angular resolutions simultaneously.

4.2. The heterodyne light field (HLF) camera

The heterodyne light field (HLF) camera is a representative of the passive-encoding technique in single-shot coded-aperture light-field imaging [153]. A prototype of this camera is shown in figure 7(a). This camera is built on a flatbed scanner [154] placed on the back of a large-format view camera fitted with a 210 mm-focal-length lens. A coded aperture with a size of 203 mm × 254 mm (i.e. 8 inches × 10 inches) is placed behind the scanner's glass surface (see the top-left image in figure 7(b)). The mask is printed at a resolution of 80 dots per millimeter using a continuous tone film recorder. The top-right image in figure 7(b) shows a part of the coded aperture. The pattern on the mask is the summation of four 2D cosine functions with different frequencies. The fundamental frequencies are $f_{0x} = f_{0y} = 1$ cycle/mm. The other three cosine functions are the harmonics (see the bottom image in figure 7(b)).

The data acquisition of the HLF camera is described by using 2D light-field formulas for simplicity (figure 7(c)). The full 4D description can be easily extended from this derivation. A band-limited scene is represented in the light field as $I(x, \theta)$. Its Fourier transform thus satisfies $\tilde{I}(f_x, f_\theta) = 0$, when $|f_x| \geqslant f_{cx}$ and $|f_\theta| \geqslant f_{c\theta}$, where f_{cx} and $f_{c\theta}$ are the cut-off frequencies in the Fourier light-field domain. $I(x, \theta)$ is multiplied by the coded aperture. This encoded scene then propagates to the sensor. In the Fourier light-field domain, this process can be expressed as the convolution between $\tilde{I}(f_x, f_\theta)$ and the Fourier transform of the coded aperture. Light propagation shears the Fourier spectrum of the coded aperture (see the top image in figure 7(c)) with a tilt angle of $\alpha_t = \tan^{-1}\left[l_{MS}/(l_{LS} - l_{MS})\right]$. The separation of adjacent δ functions is $f_0 = \mu\sqrt{4f_{cx}^2 + f_{\theta R}^2}$, where $\mu = 1/\sqrt{\left(l_{MS}/l_{LS}\right)^2 + \left[1 - \left(l_{MS}/l_{LS}\right)\right]^2}$ is a scaling factor, and $f_{\theta R}$ indicates the angular resolution of the light-field measurement. Therefore, the result of this convolution will be several spectral replicas of the light field along the slanted line (see the middle image in figure 7(d)). Finally, the sensor captures this encoded light field. This process retains only a slice of the light field in the Fourier domain [155]. Because the duplicated spectra are shifted angularly by the tilted angle α_t, different slices of the light field are captured by the sensor, which enables reconstructing the full light-field datacube (see the bottom image in figure 7(c)). Overall, the image formation process can be expressed by in Fourier domain by

$$\tilde{E}(f) = \sum_{k=-4}^{4} \tilde{I}(f - kf_0) \text{ for } |f_\theta| \leqslant f_{\theta R}/2. \tag{4-2}$$

Here $\tilde{E}$ is the Fourier transform of the captured snapshot. Figure 7(d) shows an image captured using the HLF camera. A zoomed-in view (marked by the green box in figure 7(d)) shows the attenuation of the sensor image due to the coded aperture.

In image reconstruction, the captured snapshot is Fourier transformed, which creates 9 × 9 spectral tiles due to the modulation by the cosine coded aperture (figure 7(e)). These spectral tiles encode the information about the angular variation in the light field. Each tile is filtered out, shifted to the center, and inversely Fourier transformed to produce a perspective view of the light-field image. In this way, the HLF camera recovers a 4D dataset with a size of 181 × 228 × 9 × 9 pixels.

The HLF camera provides an enhanced depth of focus. In the example shown in figure 7(d), only the orange cone on the right is in focus in the acquired data. In contrast, the reconstructed image can be digitally focused to the front, to the back, or over the entire scene (figure 7(f)). The horizontal black line in the third and the fourth panels in figure 7(f) depicts the small parallax between the views, being tangent to the white circle on the purple cone (indicated by the white arrows in figure 7(f)) in the right image but not in the left image.

The HLF camera uses an attenuating coded aperture to reversibly modulate the 4D light field. Although demonstrated with a flatbed scanner in the prototype, the data acquisition of the HLF camera can be well implemented with a 2D camera in one exposure, making it the first design of a single-shot light field camera that does not use any additional refractive elements [153]. Unlike the traditional light-field imaging apparatus [156, 157], no microlens array is used in the HLF prototype [158]. Combined with the Fourier slice theorem [155], this coded-aperture-equipped system focuses just as a traditional camera to capture a single conventional 2D image at the full sensor resolution, a capability with great potential to be adapted to other imaging platforms.

5. Temporal imaging

Single-shot coded-aperture temporal imaging is a research area of rising interest. The detection of time-of-arrival used to be seldom performed due to the limited detection bandwidth of sensors. In recent years, however, significant advances in ultrafast laser systems [159], ultrafast detectors [160–164], and new computational frameworks in imaging science [165, 166] have been applied in conjunction with coded apertures to enable observing transient phenomena with imaging speeds at the trillion-frame-per-second level in real time [167]. Among active-encoding approaches, a pinhole array is used with a lens to control both the intensity and the incident angles of pulses that probe a transient scene. The detector

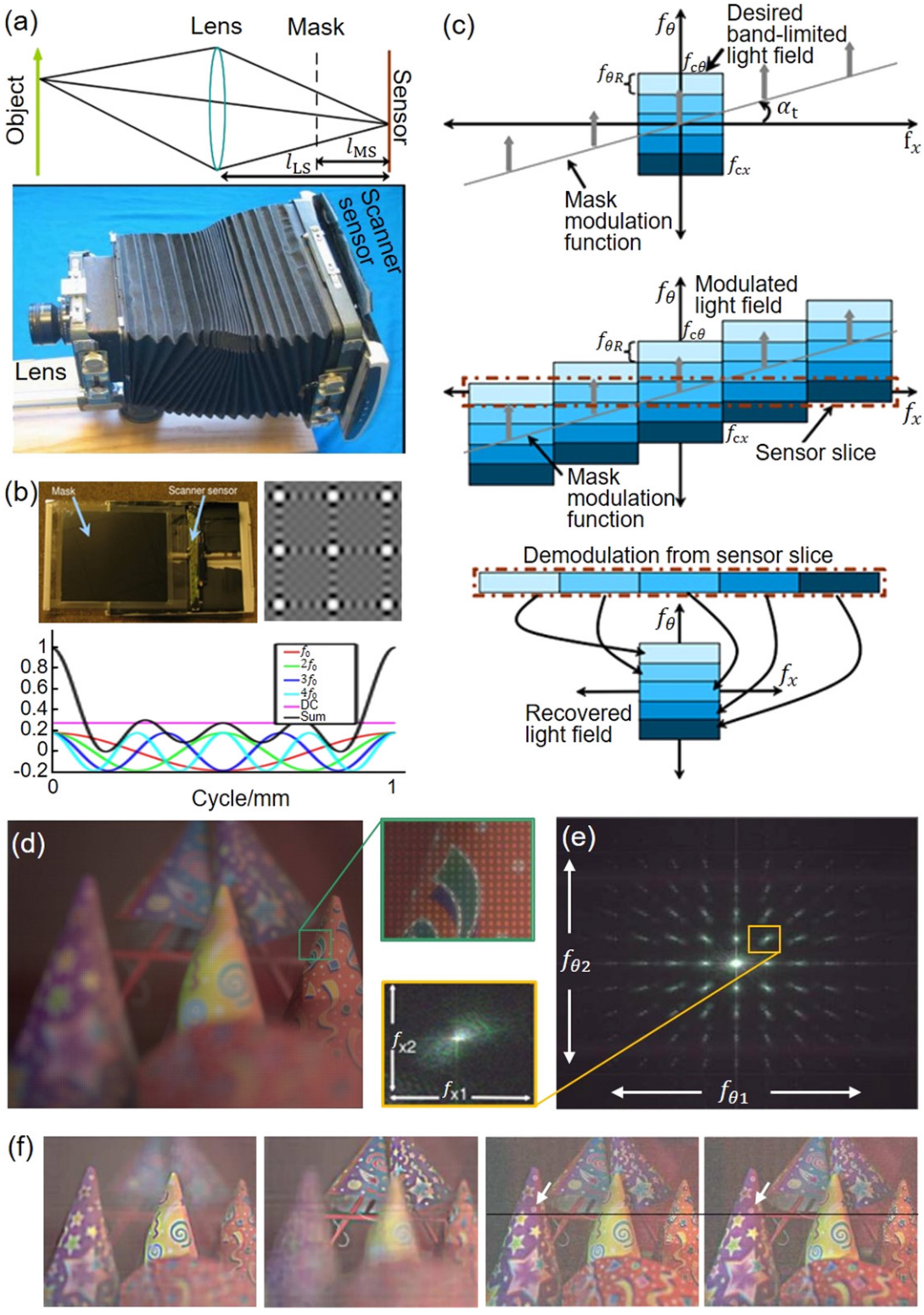

Figure 7. Heterodyne light field (HLF) camera. (a) Design and prototype. (b) Top left: arrangement of the coded aperture and the sensor. Top right: zoomed-in view of a part of the coded aperture. Bottom: 1D illustration of the coded aperture as a summation of four cosine harmonics and a constant term. (c) Image formation of the heterodyne light field camera. (d) A captured image with a zoomed-in view of a local area. (e) Fourier transform of (d) and a zoomed-in image of a perspective view. (f) Reconstructed images. First and second panels: near-focused and far-focused images. Third and fourth panels: parallax between the two selected prospect views with all of the scene in focus. A local feature is pointed out by the white arrows. Adapted with permission from [153]. © Association for Computing Machinery 2007.

records the angularly encoded information in a single shot. The temporal information can be extracted by ptychography [168, 169]. As another method, represented by the frequency recognition algorithm for multiple exposures (FRAME) technique, different carrier frequencies can be attached to individual incident pulses to probe the transient scene [170, 171]. The detector records the multiplexed data and separates the temporal information in the Fourier domain. Among passive-encoding approaches, popular methods include spatial encoding by a static pseudo-random binary mask [172], temporal encoding by using varied camera exposure with a lenslet array [173, 174], and spatiotemporal encoding by using a fast-moving transmissive mask [175, 176].

5.1. Sequentially timed all-optical mapping photography (STAMP)

Sequentially timed all-optical mapping photography (STAMP) is a representative active-encoding approach in single-shot coded-aperture temporal imaging [177]. The STAMP system, shown in figure 8(a), consists of an ultrafast pulse source, a temporal mapping device, a spatial mapping device, and an imaging sensor. In data acquisition, a femtosecond pulse generated by the ultrafast pulse source enters the temporal mapping device, which consists of a temporal disperser and a pulse shaper. The temporal disperser (e.g. a glass rod and/or an optical fiber) first stretches the pulse to a certain pulse width according to the requirement of the specific study, then this temporally stretched pulse is encoded by a pulse shaper (figure 8(b)). In particular, the first polarized beam splitter ensures the linear polarization of a pulse entering the shaper. The pulse is then spatially dispersed by a 600 lines/mm diffraction grating. Afterward, the pulse passes through a cylindrical lens and a half-wave plate, which focuses each wavelength to a different spatial point on a 128-element transmissive SLM at a 45° polarization angle. The SLM modulates the phase over the spectrum individually, which transfers to the changes in polarization of each spectral unit. The modulation after the SLM mirrors the preceding process. In this way, this temporal modulation unit produces six daughter pulses with equal amplitudes to probe the transient scene. The transmitted pulses go through the spatial mapping unit, which uses a diffraction grating and imaging optics to separate them in space. Finally, these pulses are recorded in different areas on a camera. In total, STAMP can record six frames, each of which has 450 × 450 (x, y) pixels.

STAMP's image reconstruction consists of three steps. First, the captured six frames are clipped from the captured single snapshot to produce a movie. Second, to compensate for the degradation in image contrast and background noise, each frame is pixel-wisely divided by a reference frame obtained without an excitation pulse. Finally, to further reduce noise and to enhance the signal-to-background contrast, other filters (e.g. high-pass filters) are applied to the compensated frames.

STAMP's frame rate is equivalent to the reciprocal of the temporal gap between adjacent daughter pulses, which is given by [178]

$$R = (D_{\mathrm{d}} z_{\mathrm{d}} \Delta\lambda_{\mathrm{FI}})^{-1}, \tag{5-1}$$

where D_{d} is the dispersion parameter, z_{d} is the pulse's propagation length through the dispersive element, and $\Delta\lambda_{\mathrm{FI}}$ is the difference between the center wavelengths of adjacent daughter pluses (the subscript 'FI' refers to 'frame interval'). In addition, the time-domain full-width-at-half-maximum (FWHM) width of each daughter pulse is given by

$$\tau = \sqrt{\left(\frac{2\Lambda_{\mathrm{c}}^2 \ln 2}{\pi c \Delta\lambda_{\mathrm{ET}}}\right)^2 + (D_{\mathrm{d}} z_{\mathrm{d}} \Delta\lambda_{\mathrm{ET}})^2}, \tag{5-2}$$

where Λ_{c} is the center wavelength of the pulse from the optical source, $\Delta\lambda_{\mathrm{ET}}$ is the bandwidth of the daughter pulse (the subscript 'ET' refers to 'exposure time'), and c is the speed of light in vacuum. These two terms inside the square root in equation (5-2) correspond to the Fourier-transform limit and the effect of the temporal dispersion by the temporal mapping device.

$\Delta\lambda_{\mathrm{FI}}$ and $\Delta\lambda_{\mathrm{ET}}$ needs to be deliberately chosen to balance the temporal dispersion and the transform limit. For large $\Delta\lambda_{\mathrm{FI}}$ values, $\Delta\lambda_{\mathrm{ET}}$ can be chosen to make $\tau \leqslant R^{-1}$, while for small $\Delta\lambda_{\mathrm{FI}}$ values, τ always exceeds R^{-1}, resulting in a temporal overlap between adjacent frames and hence causing a relatively large degree of motion blur. In the demonstrated configuration [177], STAMP achieved a tunable imaging speed of up to $R = 4.37$ trillion fps with a temporal resolution of $\tau = 733$ fs.

STAMP has been applied to visualizing light-induced phonon propagation in materials. A 70 fs, 40 μJ laser pulse was cylindrically focused into a ferroelectric crystal wafer at room temperature to produce coherent phonon-polariton waves (figure 8(c)). In the recovered movie with an imaging speed of $R = 1.23$ trillion fps (figure 8(d)), the first two frames show the irregular and complex electronic response of the excited region in the crystal at $t < 1$ ps [179, 180]. The following frames show an upward-propagating coherent vibration wave. At $t > 1$ ps, phonon-polariton waves are produced by impulsive stimulated Raman scattering and then propagate in the crystal in the upper direction, leaving the electronic response behind [181]. Movies were then taken with a finer frame interval of $R^{-1} = 229$ fs. The analysis of intensity profiles in these frames (figure 8(e)) revealed a propagation speed of 4.6×10^7 m s^{-1}. The FWHM temporal width, central frequency, and FWHM bandwidth of the pulse (averaged over all frames) were found to be 337 fs, 1.39 THz, and 0.99 THz, respectively.

STAMP uses a coded aperture to stamp each temporal frame with different spectral information. This technique can be easily integrated into existing spectroscopic apparatus, such as a wavelength-selective switch [182], a computed tomography imaging spectrometer [183], or an image mapping spectrometer [184]. By leveraging the broad spectrum in ultrashort laser pulses, STAMP exhibits one of the highest imaging speeds among the active-encoding approaches to single-shot coded-aperture temporal imaging. However, constrained by temporal Fourier transformation, this method has an inevitable trade-off between the temporal resolution and the sequence depth (i.e. the maximum number of frames in each reconstructed movie). These parameters can be optimized when

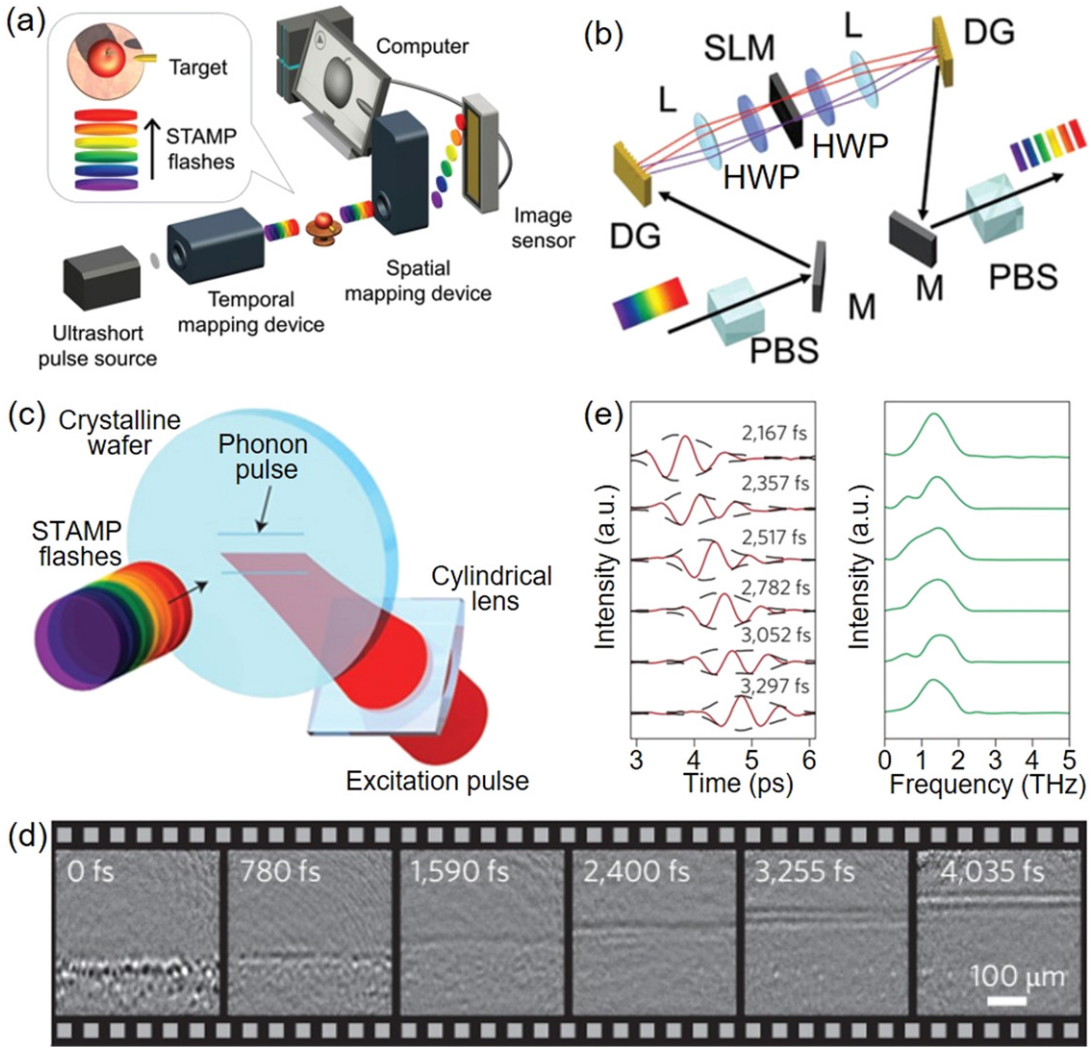

Figure 8. Sequentially time all-optical mapping photography (STAMP). (a) System schematic. (b) Schematic of the pulse shaper. DG, diffraction grating; HWP, half-wave plate; L, lens; M, mirror; PBS, polarized beam splitter. (c) Experimental schematic of observing lattice vibrational waves with STAMP. (d) A STAMP movie at 1.23 trillion fps, showing the generation and propagation of lattice vibrational waves. (e) Temporal waveforms with its carrier-envelope (marked by the black dashed lines) and corresponding spectra of the propagating phonon pulse imaged at 4.37 trillion fps. Adapted by permission from Springer Nature Customer Service Centre GmbH: Nature Photonics [177] © 2014.

$\mathrm{d}\tau/\mathrm{d}\Delta\lambda_{\mathrm{ET}} = 0$ [178]. Under this scenario, it is estimated that by using a total bandwidth of ~200 nm, $\Delta\lambda_{\mathrm{ET}} = \sim 2$ nm, and $D_{\mathrm{d}}z_{\mathrm{d}} = 0.1\ \mathrm{ps\,nm^{-1}}$, it would be possible to achieve a total of ~100 frames with ~200 × 200 (x, y) pixels per frame at a frame rate of 5 trillion fps.

5.2. Compressed ultrafast photography (CUP)

Among the passive-encoding approaches to single-shot coded-aperture temporal imaging, one representative technique is compressed ultrafast photography (CUP) [185]. The schematic of the first-generation CUP system is shown in figure 9(a). In data acquisition, the dynamic scene, denoted as $I(x, y, t)$, is first imaged by a camera lens to the intermediate image plane. Afterward, the light passes through a beam splitter and is imaged to a DMD through a 4f system consisting of a tube lens and an objective lens. A pseudo-random binary pattern is loaded onto the DMD for spatial encoding. The light reflected by the 'ON' pixels on the DMD is collected by the same 4f system so that a spatially encoded dynamic scene is relayed via the reflection of the beam splitter to the fully-opened entrance port (5 mm × 17 mm) of a streak camera. After passing through this port, the image is further relayed by input optics onto a photocathode, where photons are converted into photoelectrons via the photoelectric effect. These photoelectrons are accelerated by a pulling voltage and then passed between a pair of sweep electrodes. A linear voltage ramp is applied to the electrodes so that the photoelectrons are deflected to different vertical positions (along the y'' axis in figure 9(a)) according to their times of arrival. This operation temporally shears the spatially encoded scene. The deflected photoelectrons are amplified by a micro-channel plate and then converted back to photons by bombarding a phosphor screen. The image of the phosphor screen is relayed by output optics to an internal imaging camera with a size of $N_{\mathrm{h}} \times N_{\mathrm{v}}$ pixels (where the subscripts 'h' and 'v' denote 'horizontal'

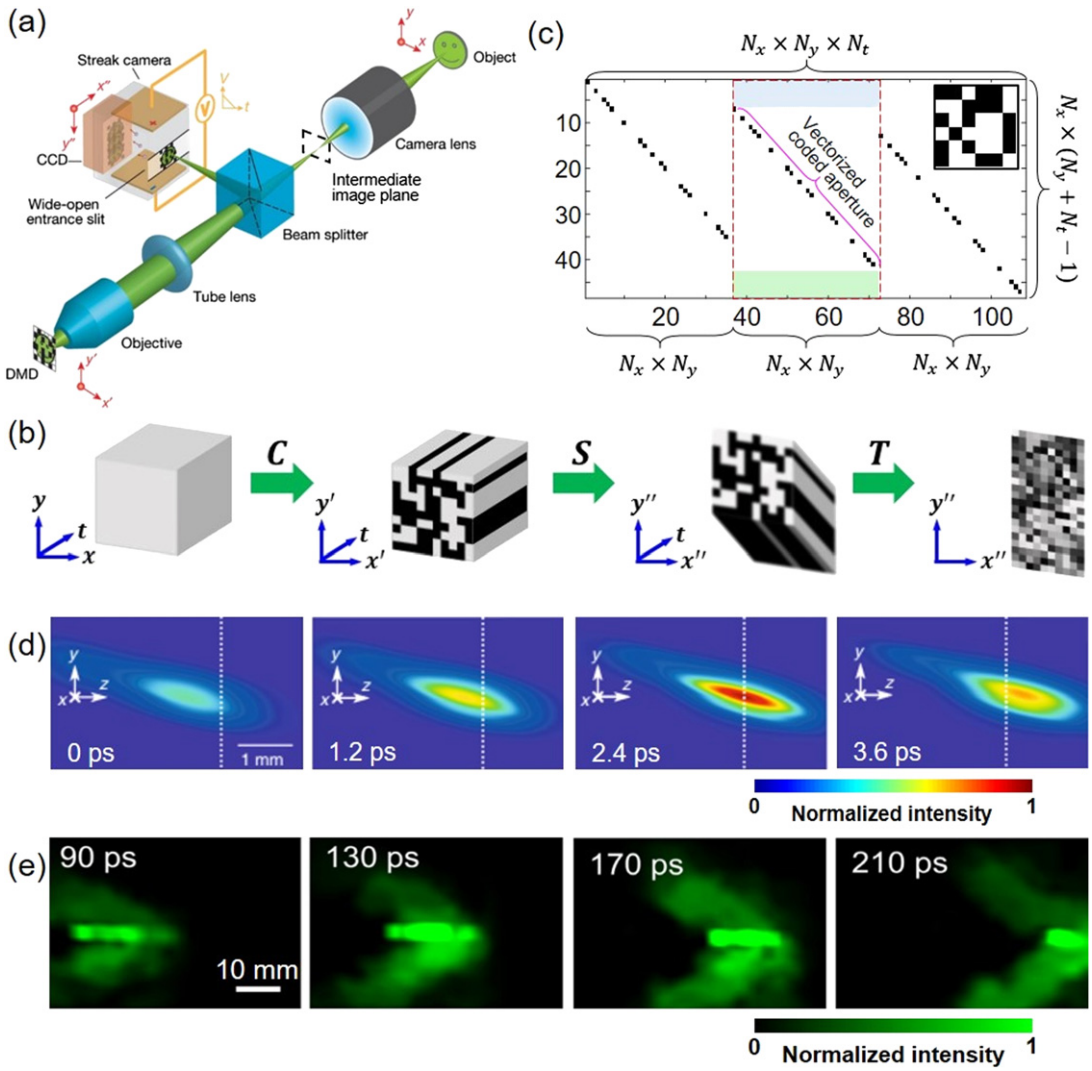

Figure 9. Compressed ultrafast photography (CUP). (a) Schematic of the first-generation CUP system. (b) Illustration of data acquisition in CUP. (c) CUP's sensing matrix. (d) Single-shot T-CUP of temporal focusing of a femtosecond laser pulse at 2.5 trillion fps. (e) Single-shot LLE–CUP of a propagating photonic Mach cone at 100 billion fps. (a) Adapted by permission from Springer Nature Customer Service Centre GmbH: Nature [185] © 2014. (b) and (d) From [197]. Adapted with permission from AAAS. (e) Adapted by permission from Springer Nature Customer Service Centre GmbH: Springer [196] © 2018.

and 'vertical', respectively). Via this spatiotemporal integration, the spatially encoded and temporally sheared datacube is compressively recorded as a single snapshot, denoted as $E(m,n)$, where m and n stand for the indices of pixels in the horizontal and vertical directions of the internal camera. In this regard, the data acquisition of CUP can be expressed by (figure 9(b))

$$E(m,n) = \boldsymbol{TSC}I(x,y,t), \tag{5-3}$$

where the three operators, $\boldsymbol{C}$, $\boldsymbol{S}$, and $\boldsymbol{T}$, represent the operations of spatial encoding, temporal shearing, and spatiotemporal integration, respectively. To assure good sensing performance, the coded aperture and the associated sensing matrix need to be incoherent with respect to the sparse basis that represents the scene. Because random matrices are largely incoherent with any fixed basis [186], they are used as a universal coded aperture in CUP. If the numbers of pixels in the spatiotemporal (x,y,t) cube of the dynamic scene are N_x, N_y, and N_t, the numbers of pixels in the captured snapshot should satisfy $N_x \leqslant N_{\mathrm{h}}$ and $N_y + N_t - 1 \leqslant N_{\mathrm{v}}$.

CUP's data acquisition is further illustrated using a matrix-vector expression. For simplicity, the following assumptions are made: first, the PSF is perfect over the entire FOV. Second, the shearing by the voltage ramp of the streak camera is linear. Finally, there is a one-to-one mapping of the elements of the aperture code to the detector pixels. These assumptions make it easy to interpret CUP measurement as a linear process. As an example, a datacube size of $N_x = N_y = 6$ and $N_t = 3$ is used. A 6×6 pseudo-random binary pattern is illustrated in the inset of figure 9(c). The sensing matrix of CUP is constructed by sequentially multiplying the matrices of three operations in the data acquisition. The final matrix consists of N_t sub-matrices. Each sub-matrix (marked by the red dashed box in figure 9(c)), with a size of $\left[N_x \times (N_y + N_t - 1)\right] \times \left(N_x \times N_y\right)$, has a structure that can be decomposed as follows. First, a

diagonal pattern, formed by vectorizing the coded aperture, repeats in each sub-matrix. In addition, $N_x \times (n_t - 1)$ rows are appended above this diagonal matrix (light-blue shaded in figure 9(c)). Finally, $N_x \times (N_t - n_t)$ rows are appended below this diagonal matrix (light-green shaded in figure 9(c)). Here, $n_t = 1, 2, \ldots, N_t$ stands for the index of frames. Experimentally, the sensing matrix was assembled by calibration. The coded aperture is first measured. Ensuing processing compensates for various non-idealities, including the spatially varied PSF, non-linearity in shearing, non-uniform spectral sensitivity, and subpixel misalignments between the aperture code features and detector pixels.

CUP's image reconstruction can be formulated by

$$\hat{I} = \arg\min_{I} \left\{ \frac{1}{2} \|E - \boldsymbol{TSC}I\|_2^2 + \beta \Phi_{\mathrm{TV}}(I) \right\}, \qquad (5\text{-}4)$$

where $\Phi_{\mathrm{TV}}(\cdot)$ is a regularization function of the total variation (TV) that promotes sparsity in the dynamic scene, and β is the regularization parameter. The solution to this minimization problem can be stably and accurately recovered, even with a highly compressed measurement [187]. In practice, equation (5-4) can be solved by various methods, including the two-step iterative shrinkage/thresholding algorithm [188], alternating direction method of multipliers algorithm [189], and augmented Lagrangian algorithm [190]. For the first-generation CUP system, the reconstruction produced up to 350 frames in a movie, with an imaging speed of up to 100 billion fps. Each frame contained 150 × 150 (x, y) pixels, and the temporal resolution was quantified to be ∼50 ps [191].

The coded aperture used in CUP can be optimized to improve the system's performance. The number of needed pixels in the acquired snapshot is proportional to the product of the coherence, the number of non-zero elements in the sparse representation, and the number of voxels in the datacube [192]. Based on this relation, CUP has been optimized by three methods. The first method minimizes the mutual coherence between the sensing matrix and the representation basis of the scene, including using the genetic algorithm [193] and the gradient descent algorithm [194]. The second method is to increase the sparsity of the scene by transforming the scene into another basis (e.g. the Fourier basis) [195]. Third, several designs have been implemented in hardware to increase the number of measured pixels by improving the detection capability of the CUP system. As an example, an external CCD camera was added to capture a time-unsheared view [196]. Accompanied by a femtosecond streak camera, this innovation contributed to the development of trillion-frame-per-second CUP (T-CUP), with an imaging speed of 10 trillion fps. Another design, termed lossless-encoding (LLE)–CUP, implements complementary encoding masks from the DMD [197]. Finally, multi-encoding schemes, which first generate multiple replicas of the scene and then use different masks for spatial encoding, can be implemented [174].

As a universal imaging platform, CUP has found widespread applications. For example, the ToF–CUP has enabled single-shot encrypted volumetric imaging at 75 volumes per second [198]. This work was further extended to secure optical communication [199]. In addition, CUP has achieved single-shot fluorescence lifetime mapping [185, 200] by recording both the excitation and the fluorescence emission processes. Recently, the imaging capability of CUP has been extended to phase-contrast [201] and hyperspectral sensing [202]. Finally, the concept of CUP has been implemented with off-the-shelf CCD and CMOS cameras [172], with transmission electron microscopes [194, 203], and with active illumination [204, 205].

Among these applications, CUP has been most popularly used to image light dynamics. As an example, figure 9(d) shows four representative images of the full evolution of the temporal focusing of a femtosecond laser pulse, imaged by T-CUP at 2.5 trillion fps in a single shot. A spatially chirped pulse with a tilt angle of ∼76° propagates toward the right. The pulse width continuously narrows, resulting in an increasing intensity that peaks at the temporal focusing plane (see the third panel in figure 9(d)). After that, the pulse width is elongated, resulting in a continuously weakened intensity. As another example, figure 9(e) shows four frames of a video of a photonic Mach cone, imaged by LLE–CUP at 100 billion fps. This superluminal event was induced by propagating a picosecond laser pulse in a scattering panel assembled by materials with different refractive indices. The movie produced by LLE–CUP revealed the generation and ensuing propagation of a photonic Mach cone. The cone edges are seen as two light tails extending from the tip of the propagating laser pulse, forming a V-shaped wedge with a semi-vertex angle of 45°.

In summary, CUP is a novel single-shot coded-aperture temporal imaging modality with many advantages. Conceptually, CUP synergistically combines compressed sensing with streak imaging. Despite using a single, static coded aperture, the temporal shearing operation smears the spatially encoded frames, which preserves the temporal information in the compressively recorded snapshot. This unique scheme adds another spatial dimension in streak cameras. It also offers a large sequence depth (typically 300 to 1000 frames) in the reconstructed movies. However, the spatiotemporal mixture in CUP trades spatial resolution and resolution isotropy for temporal resolution and the added spatial dimension [185].

6. Spectral imaging

Single-shot coded-aperture spectral imaging has received an increasing amount of attention in recent years [206]. Its broad applications have included monitoring of cellular metabolism, detection of disease in early stages, and non-contact analysis of chemical composition for forensics [207–210]. Numerous types of coded apertures have been developed for single-shot spectral imaging. For example, SLMs are commonly used to project sparse illumination for parallel and label-free micro-spectroscopy [211, 212]. As another example, various designs of coded apertures—such as pinhole arrays [213], lenslet arrays [214], and dimensional-reduction fiber couplers [215]—are used to generate blank regions on the sensor to record the spectral information. Moreover, many color-filter arrays (e.g. the Bayer mode array) have been implemented on either the illumination or detection side to encode

color information in a monochromatic sensor [216–218]. Among existing techniques, coded-aperture snapshot spectral imaging (CASSI) has been a notably active research area [219]. With a similar conceptual structure to CUP, CASSI uses spatial encoding, spectral shearing, and spatiospectral integration to compressively record an (x, y, λ) datacube in a single exposure. CASSI's development has proceeded on many fronts, including pattern optimization [220, 221], new applications in forensics and environmental studies [222], novel image reconstruction methods [223], and hardware improvement [224], and these efforts have led to CASSI's successful commercialization [225].

6.1. The Fourier-spectral-multiplexing (FSM) device

The Fourier-spectral-multiplexing (FSM) device is a representative of active-encoding approaches to single-shot coded-aperture spectral imaging [226]. In the FSM prototype shown in figure 10(a), collimated broadband light first passes through a $4f$ imaging system, in which a rotating color wheel is placed in the Fourier plane for spectral modulation. The color wheel contains six segments, whose spectra (shown in figure 10(b)) are deliberately selected to minimize their spectral correlation with one another. In addition, these filters are broadband to increase their SNRs. The filtered light is then shaped by a DMD-based band-limited projector [227]. As shown in figure 10(c), the light illuminates the DMD, on which a binary pattern is loaded. Processed by a digital halftoning algorithm [228], the Fourier spectrum of this binary pattern precisely matches the imaging content to the corresponding grayscale pattern at a limited system bandwidth. To filter the high-spatial-frequency noise, an optical low pass filter is constructed. Specifically, the reflected beam is Fourier transformed by a concave mirror back to another area of the DMD, where a pattern of three pinholes is displayed to perform spatial filtering. The filtered spectrum is Fourier transformed by another lens. In this way, a single binary pattern can be converted into a grayscale sinusoidal pattern that illuminates the sample. The generated spatiospectral (x, y, λ) scene is detected by a monochromatic camera in either reflection or transmission mode.

In data acquisition, the rotation frequency of the color wheel is set to be equal to the camera's imaging speed of 24 fps, so within each camera exposure, six sinusoidal fringes with different angles are generated by the DMD-based band-limited projector. Each sinusoidal fringe thus modulates incident light filtered by a different segment in the color wheel. In this way, six fringe patterns are incoherently added into the same snapshot. The above data formation process can be formulated by

$$E(x,y) = \sum_{i=1}^{J} \int_{\lambda} f_i(\lambda)\, I(x,y,\lambda)\, s_i(x,y)\, \mathrm{d}\lambda. \tag{6-1}$$

Here, $f_i(\lambda)$ represents the transmission spectrum of each segment in the color wheel. Further, $s_i(x,y) = [1 + \cos(\mathbf{r}\cdot\omega_i)]/2$, where $\mathbf{r} = (x, y)$ is the 2D spatial coordinates, and ω_i represents the spatial frequency of the attached sinusoidal pattern.

In image reconstruction with this device, $E(x, y)$ is transformed into the Fourier domain to separate the information carried by each sinusoidal pattern. The desired content is filtered out, shifted to the center, and inversely Fourier transformed back to the spatial domain (figure 10(d)). This process produces estimations of spectrally filtered images, $\hat{I}_{\mathrm{F}i}(x, y)$. Then, various artifacts are removed by the generalized alternating projection method [229] to improve image quality. These images link to the hyperspectral datacube $\hat{I}(x, y, \lambda)$ by $\hat{I}_{\mathrm{F}i}(x,y) = \int_{\lambda} f_i(\lambda)\, \hat{I}(x,y,\lambda)\, \mathrm{d}\lambda$.

Next, $\hat{I}(x, y, \lambda)$ is recovered by using a spectrum decomposition method [230, 231], which is based on the theory that the spectra of the natural materials can be represented as a linear summation of a few (e.g. $J = 6$) characteristic spectral bases [232], i.e.

$$I(x,y,\lambda) = \sum_{j=1}^{J} \alpha_j(x,y) b_j(\lambda), \tag{6-2}$$

where $b_j(\lambda)$ is the jth known spectral basis, and $\alpha_j(x, y)$ is the corresponding coefficient. Therefore, the spectrally filtered images can be represented by

$$\hat{I}_{\mathrm{F}i}(x,y) = \sum_{j=1}^{J} \alpha_j(x,y) F_{ij}. \tag{6-3}$$

where $F_{ij} = \int_{\lambda} f_i(\lambda)\, b_j(\lambda)\, \mathrm{d}\lambda$. $\hat{I}(x, y, \lambda)$ can be solved by the following constrained optimization

$$\arg\min_{\alpha} \|I_{\mathrm{F}} - F\alpha\|_2^2 + \eta_1 \left\| \frac{\partial^2 I(x,y,\lambda)}{\partial^2 \lambda} \right\|_2^2 \quad \text{subject to } I(x,y,\lambda) \geqslant 0. \tag{6-4}$$

Here, $I_{\mathrm{F}} = \left[\hat{I}_{\mathrm{F}1}, \hat{I}_{\mathrm{F}2}, \ldots, \hat{I}_{\mathrm{F}J}\right]^T$, $\alpha = [\alpha_1, \alpha_2, \ldots, \alpha_J]^T$, and $F = \{F_{ij}\}$. The parameter η_1 weights the spectrum smoothness.

The FSM device has been applied to imaging the diffusion process [233]. A light blue pigment and an orange one were poured sequentially into a glass of water. Figure 10(e) shows two representative images of this process. The color of the water gradually changes from light blue to a mixture of blue and orange. The sinking and mixing of these two colored pigments in the water results in a changing spectrum distribution over the diffusion process.

In the FSM device, the coded aperture attaches sinusoidal functions of different orientations to different colors into illumination. The Fourier multiplexing makes it possible to separate band-limited image content in the spatial frequency domain. In image reconstruction, the FSM device leverages both the spatial and spectral sparsities of the natural scene in a constrained optimization problem. This innovation provides the FSM device with high spatial and spectral resolutions at a video rate, along with an economical setup and a low computational workload compared with other single-shot encoded-aperture spectral imaging techniques [234–236]. The major limitation of the FSM device is the trade-off between spatial resolution and the number of color channels. The limited spatial resolution could be mitigated by using various demosaicing algorithms [237].

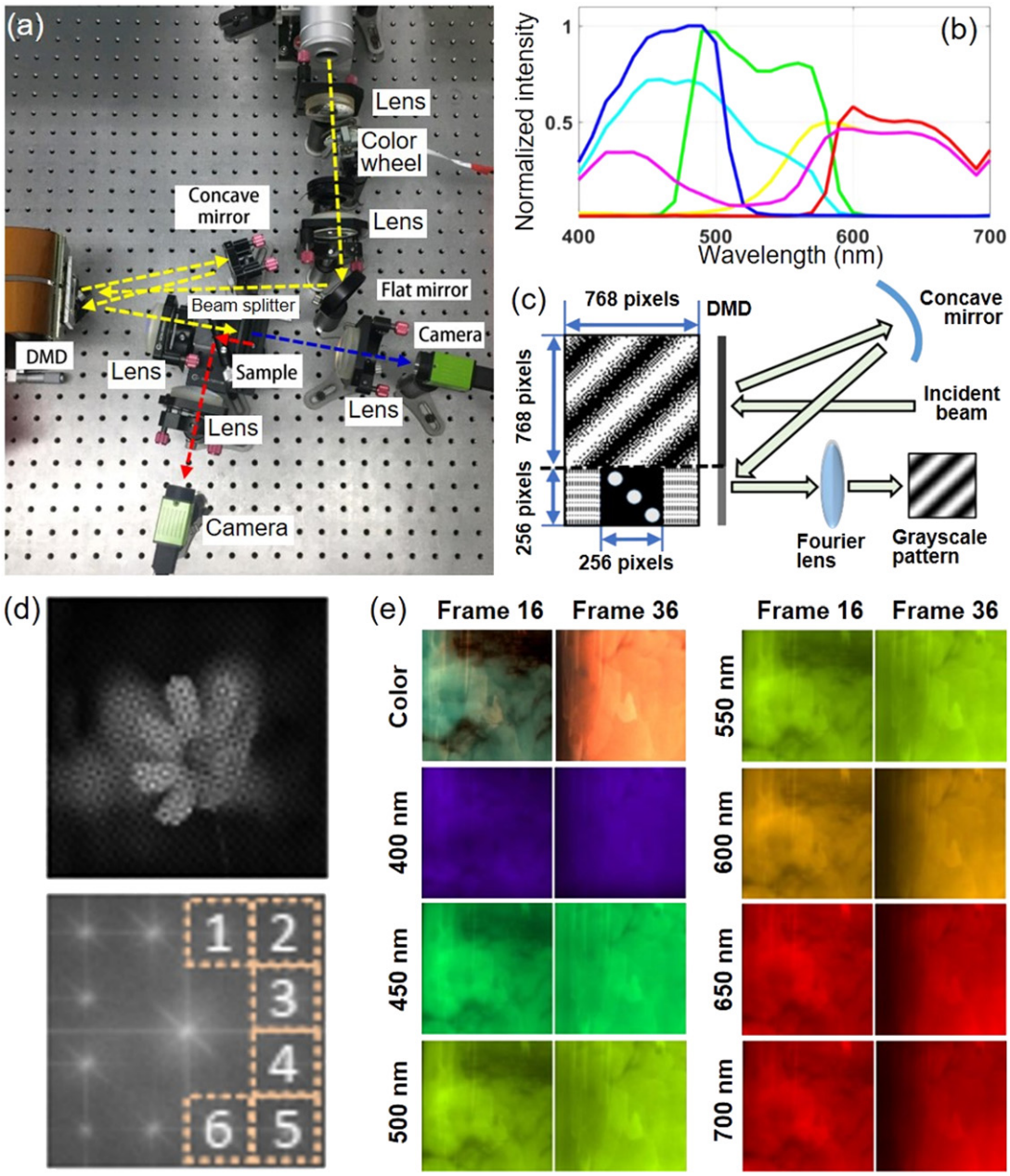

Figure 10. Fourier-spectral-multiplexing (FSM) device. (a) System schematic. (b) Transmission spectra of the six segments on the rotating color wheel. (c) Operating principle of DMD-based band-limited projection. (d) Snapshot of a flower by the FSM device (top) and its Fourier transformation (bottom). The numbered orange-dashed boxes in the bottom image mark the spatial frequency content of filtered images that are carried by the sinusoidal patterns to different regions in the Fourier domain. (e) Hyperspectral reconstruction of the diffusion of blue and orange pigments poured sequentially into water. Reproduced from [226]. CC BY 4.0.

6.2. The hyperpixel array (HPA)^{TM} camera

The hyperpixel array (HPA)^{TM} camera is a representative of passive-encoding approaches to single-shot coded-aperture spectral imaging [238, 239]. In the example system shown schematically in figure 11(a), the front optics image the scene onto a pinhole array that spatially samples the scene. The sampled image is then relayed to a CCD camera by a 4*f* imaging system, in which a prism is placed to spatially disperse the spectrum transmitted from each pinhole.

In data acquisition, the coded aperture used in the HPA camera reserves pixels on the sensor to record the spectral information. The spatial filtering by the pinhole array generates void spaces between adjacent pinhole images. In the ensuing spectral dispersion, the prism shears the spectrum at 16° with respect to the pinhole array (figure 11(b)) so that all the constituent colors in each pinhole are mapped without overlap, filling in the void spaces. An example of a captured snapshot is shown in figure 11(c).

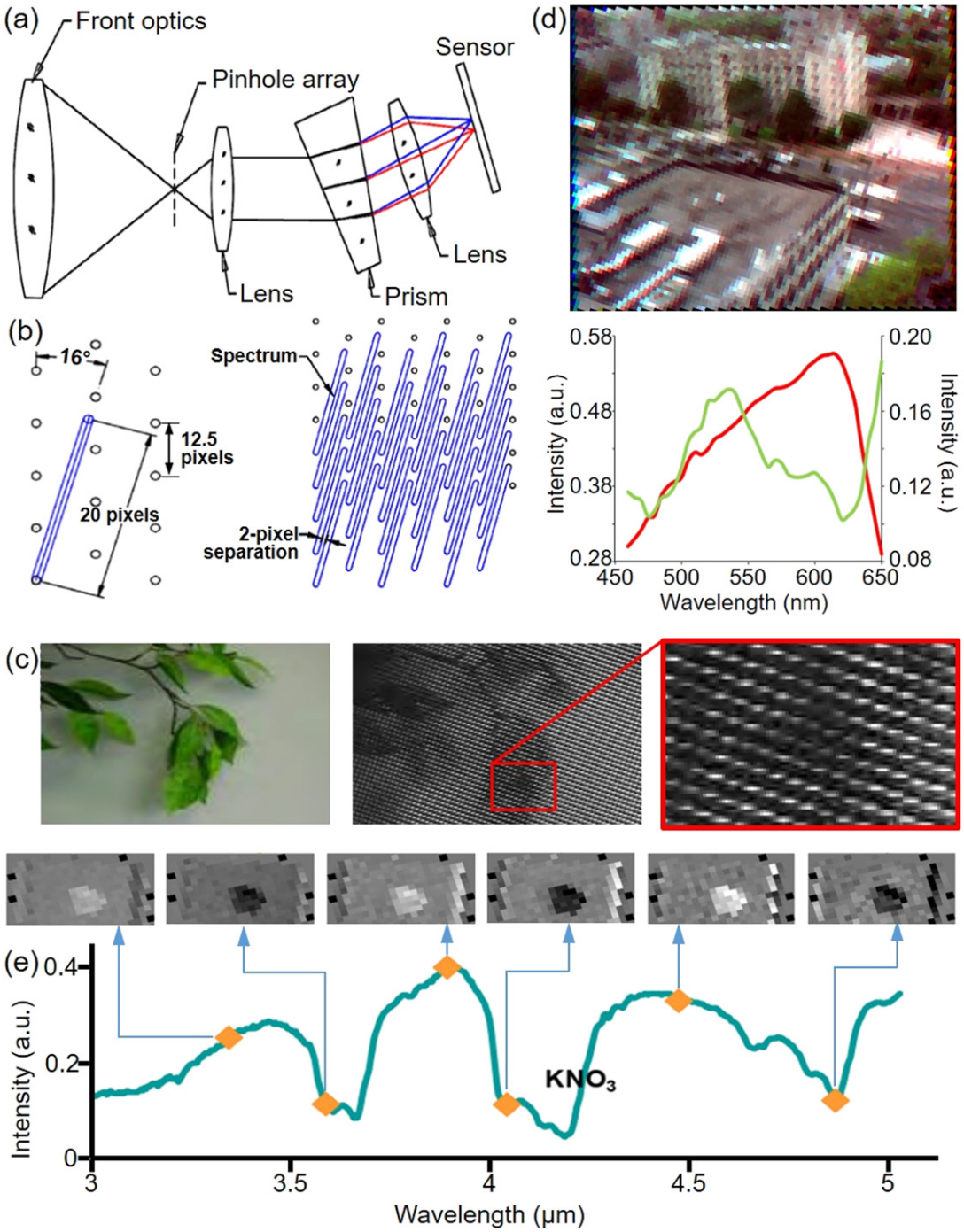

Figure 11. Hyperpixel array (HPA)^{TM} camera. (a) System schematic. (b) Left: geometry of the coded aperture. Right: illustrative intensity pattern on the sensor. (c) A hyperspectral scene (left) and the measured snapshot containing 20 visible wavelengths (middle). A zoomed-in view of a local area is shown on the right. (d) Reconstructed hyperspectral images (top) and full spectra of two selected pixels (bottom). (e) Representative (x, y) frames (top panels) at six wavelengths of a potassium nitrate (KNO_3) smudge on a steel coupon, along with the full spectrum (bottom). Adapted with permission from [238]. © (2009) COPYRIGHT Society of Photo-Optical Instrumentation Engineers (SPIE). Adapted with permission from [239]. © (2012) COPYRIGHT Society of Photo-Optical Instrumentation Engineers (SPIE).

The HPA camera is calibrated by using monochromatic light spanning the spectral range of the instrument to determine the wavelength-dependent (x, y) positions for every pinhole. Each resulting spot (excluding bad pixels) is fitted with a 2D Gaussian model to provide a more accurate location of its centroid. In this way, both the radiometric response and the pinhole-to-pinhole non-uniformity correction are determined. In image reconstruction, the calibration results are used as references to re-map the 2D spectrally sheared image back to a 3D (x, y, λ) datacube with compensated uniformity and intensity [238].

Since its initial development, the concept of the HPA camera has been realized in many different spectral bands. Figure 11(d) shows a hyperspectral datacube recorded with a visible-near-infrared HPA camera. The full spectrum of two pixels—with the coordinates $(64, 33)$ and $(64, 35)$—shows that the HPA camera can distinguish foliage from the background. Leveraging this imaging ability, the HPA camera was applied to recognizing and tracking moving objects (e.g. vessels on water) based on their spectra. The HPA camera was also used for video-rate visualization and identification of chemicals in the mid-infrared spectrum. Figure 11(e) shows several (x, y) frames at different wavelengths from a reconstructed hyperspectral datacube of a potassium nitrate (KNO_3) smudge on a steel coupon [238]. The HPA camera has clearly identified the chemical by its signature wavelengths.

Besides object recognition and chemical identification, the HPA camera has been applied for many other purposes. For example, it imaged complex chemical reactions in a plume of gas in the infrared wavelength range [238]. The spectrum information also marked temperature changes in additive and subtractive manufacturing [240]. Furthermore, this technique aided the spatiotemporal refocusing of a femtosecond laser pulse through a scattering medium [241]. Finally, it has been implemented in homeland security for counter-camouflage, denial, and deception [242].

The HPA camera offers several advantages in space-resolved spectral imaging. First, it acquires a relatively small size (x, y, λ) datacube and has a low computational load for post-processing. In addition, having a low-cost and compact size with robust performance, the HPA camera is highly adaptable for hand-held devices as well as other platforms that have restrictions for weight and size, including satellites, aircraft, and robots. However, the pinhole-array-based HPA camera has a low light throughput. This limitation has been alleviated by using a lenslet array or a fiber bundle [214, 243]. Moreover, the HPA camera has an inherent trade-off between spatial resolution and spectral resolution, which could be compensated for by deploying multiple HPA cameras as an array or by implementing compressed sensing methods [244].

7. Polarization imaging

Single-shot coded-aperture polarization imaging has emerged as a potent research direction. It allows accurate and quick analyses of light polarization to extract rich information that reflects the physical, chemical, and biological properties of the imaged environment [245–247]. In recent years, this modality has found increasing applications in diverse fields of study, including metrology, remote sensing, target discrimination, haze removal, and biomedicine [248]. Polarization can be used to encode either illumination or emission photons as another degree of freedom that contributes to novel optical imaging system designs. In active-encoding approaches, spatial sinusoids are commonly used as coded apertures to modulate light with different polarization states in single-shot optical sectioning in microscopy [249, 250]. Among passive-encoding approaches, a popular implementation is to monolithically integrate a micropolarizer array (MPA) with a camera sensor [251, 252]. In addition, SLMs [253] and patterned nanostructures [254] are used to encode light's polarization states for image encryption [255], in both coherent and incoherent imaging [256, 257].

7.1. Rheinberg polarization microscopy (RPM)

Rheinberg polarization microscopy (RPM) is an example of active-encoding-based single-shot coded-aperture polarization imaging [258]. In the system shown in figure 12(a), a liquid-crystal-display (LCD) projector is coupled to an upright microscope by intermediary lenses. A designed coded aperture pattern is projected onto the back focal plane of the condenser lens so that light with different polarization states illuminates the sample at different angles. The employed LCD projector has three color channels (inset in figure 12(a)) that emit linearly polarized light. The red and blue color constituents have the same linear polarization and are mutually perpendicular to the green component. An analyzer is placed after the objective lens to sense the polarization information of the specimen. The analyzer is oriented orthogonal to the green illumination, so that only red and blue are detected in the absence of any birefringent material. In this way, Rheinberg imaging and polarization imaging are achieved simultaneously using a single coded aperture.

RPM has been deployed to extract birefringent structures in biological samples (figure 12(b)). The coded aperture (see the inset in figure 12(b)) contains a red annular ring and a green background. The white, red, and green arrows show the polarization direction of the analyzer and the two emitted lights. The sample is a translucent *lily anther*. The red in the image shows the non-birefringent pollen sac and parts of the membrane. In contrast, the green depicts the birefringent fibrous membrane and the pollen sacs where mitotic and meiotic cells that normally contain filamentous mitotic spindles are present [259]. The dark background enables a polarization contrast ratio of 100:1.

RPM has also enabled structure-dependent polarization imaging. To achieve this function, two geometries of coded apertures were designed to pass polarized light. When the cross-polarized light was used as a background, the system probed birefringence from the zeroth-order scattering (see the top image of figure 12(c)). This configuration allowed demarcating birefringence from low spatial frequencies (in green) from the non-birefringent counterparts (in black and blue). When the cross-polarized light passed through the annular

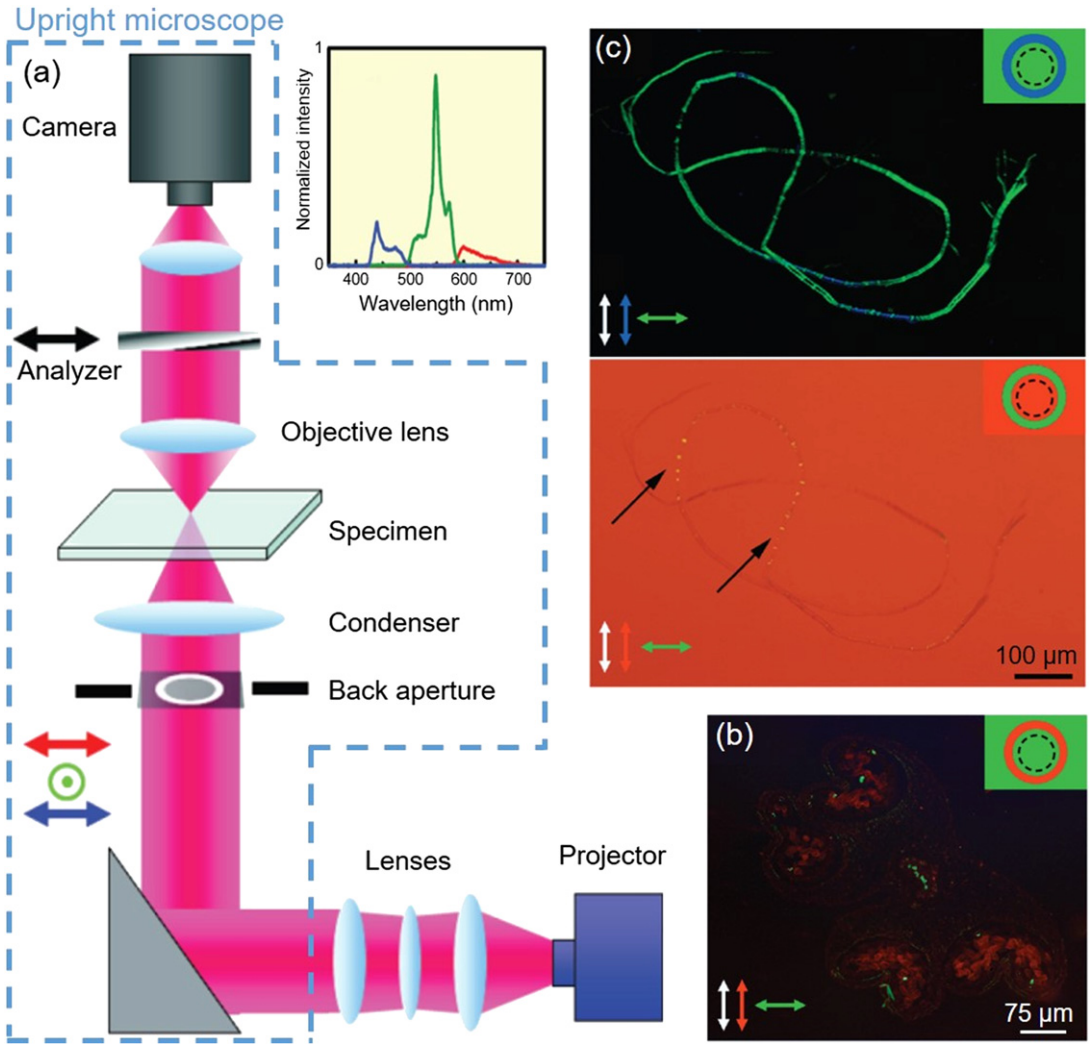

Figure 12. Rheinberg polarization microscopy (RPM). (a) System setup. (b) Simultaneous polarization and Rheinberg imaging of a *lily anther*, showing differential staining of birefringent (green) and non-birefringent sites (red). (c) Active isolation of birefringence and non-birefringence on structures with low (top) or high (bottom) spatial frequencies. Reproduced from [258]. CC BY 4.0.

ring, the system probed birefringence from higher-order scattering. In the bottom image of figure 12(c), the red background is non-birefringent. Darker outlines in the sample are produced by birefringent filaments, with, however, low scattering. Birefringence at high spatial frequencies is shown in the yellow regions (indicated by the black arrows in the bottom image of figure 12(c)). In this way, this system separates birefringence emanating from different spatial frequencies.

In summary, RPM achieves simultaneous polarization imaging and optical staining of complementary structures. The projection takes advantage of the polarized light of each primary color coming from the LCD projector itself. The acquired images, reflecting the true colors that are optically stained on the sample, do not require either image superposition or filtering. The complexity and flexibility of the coded aperture can be further enhanced by using polarized LED arrays [260, 261].

7.2. The micropolarizer array (MPA)-filtered CCD camera

The MPA-filtered CCD camera is a representative of passive-encoding approaches to single-shot coded-aperture polarization imaging [262]. In the system shown in figure 13(a), the MPA itself consists of repeated groups, each containing four pixelated linear polarization filters oriented at 0°, 45°, 90°, and 135°. Each filter, matched in size to the photodiode underneath, is composed of aluminum nanowires with a 70 nm width, 140 nm pitch, and 110 nm height [263]. Directly deposited on the surface of the imaging sensor, these filters are made in a series of optimized nanofabrication steps: interference lithography, metal and dielectric deposition, and reactive ion etching [263]. Overall, this coded aperture functions as a spatially varied polarization filter. In data acquisition, the acquired snapshot contains four sub-frames, denoted by $E_{0°}$, $E_{45°}$, $E_{90°}$, and $E_{135°}$. Subsequently, these sub-frames are interpolated to regain the lost spatial resolution [264, 265].

The image reconstruction process uses the captured snapshot to recover the angle of polarization (AoP) and the degree of linear polarization (DoLP) [247]. In particular, the four sub-frames are used to calculate the first three Stokes parameters

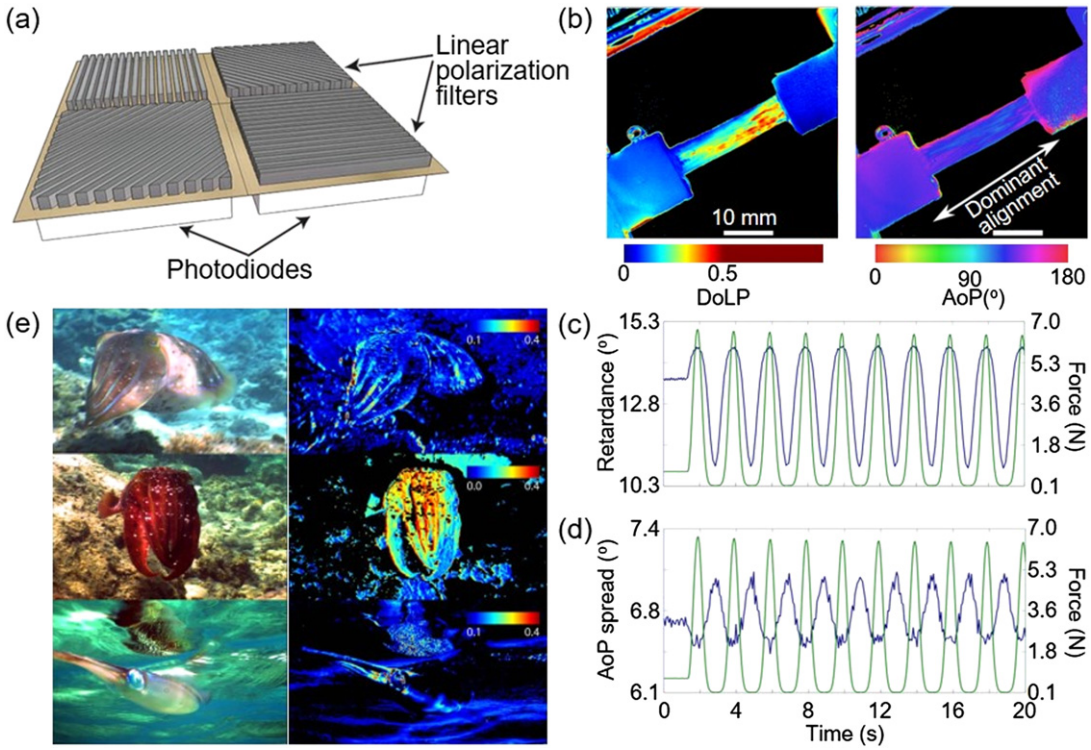

Figure 13. Micropolarizer array (MPA)-filtered CCD camera. (a) Structure of an array that contains four photodiodes, each of which is covered by a linear polarization filter with a different angle. (b) Single-shot images of DoLP (left) and AoP (right) of a bovine tendon. (c) Time course of retardance in cyclic loading of force at 0.5 Hz. (d) As (c), but showing AoP spread. (e) Representative color images (left column) and corresponding DoLP images (right column) of *S. latimanus* (top and middle) and *S. lessoniana* (bottom). (a) © 2017 IEEE. Adapted with permission, from [262]. (b)–(d) Adapted with permission from [268]. © SPIE 2014. (e) Reproduced from [248]. CC BY 4.0.

by

$$\begin{aligned} S_0 &= E_{0^\circ} + E_{90^\circ}, \\ S_1 &= E_{0^\circ} - E_{90^\circ}, \text{ and} \\ S_2 &= E_{45^\circ} - E_{135^\circ}. \end{aligned} \tag{7-1}$$

Then, AoP and DoLP are computed as

$$\begin{aligned} \text{AoP} &= \frac{1}{2}\tan^{-1}\left(\frac{S_2}{S_1}\right), \text{ and} \\ \text{DoLP} &= \frac{\sqrt{S_1^2 + S_2^2}}{S_0}. \end{aligned} \tag{7-2}$$

MPA-filtered CCD cameras have been popularly applied in biomedicine [266, 267]. As an example, figures 13(b)–(d) illustrate the real-time high-resolution measurement of collagen alignment in dynamically loaded soft tissue [268]. Circularly polarized light illuminated a bovine flexor tendon mounted on a computer-controlled actuator and a six-degree-of-freedom sensor stage. The transmitted light was captured by the MPA-filtered CCD camera. Under this setting, the angle of alignment θ and the retardance ϕ of the tissue sample were linked with AoP and DoLP by $\theta = \text{AoP} + 45^\circ$ and $\phi = \sin^{-1}(\text{DoLP})$. Figure 13(b) shows that the averaged alignment angle of tissue is at 122.9°, with a spread of 6.78°. In addition, the single-shot imaging capability enabled analysis of rapid movement. In particular, the actuator cyclically loaded the tendon to between 2% and 3% strain at rates of 0.5, 1, and 2 Hz. The time histories of the average DoLP and the spatial angular deviation of the AoP over the tendon area were compared with the loaded forces (figures 13(c) and (d)). Under conditions of high strain, the retardance was at the maximum, and the spread of the AoP cycled to the minimum. The converse occurred during periods of low strain. This behavior was expected because the fibers were more aligned when pulled.

The MPA has also been used with a color camera in the study of marine biology [248]. Figure 13(e) shows the snapshots of two marine animals (i.e. *Sepia latimanus*, a cuttlefish, and *Sepioteuthis lessoniana*, a squid) imaged in their natural habitats. These animals exhibited polarization and color signatures on their bodies. The simultaneous recording of color and polarization enabled analyzing wavelength-dependent DoLP. For the blue and red channels, the difference was 6%–10%.

The MPA-filtered CCD cameras offer several advantages. First, because the coded aperture is placed at the sensor plane, the MPA can be integrated into a variety of cameras to enable single-shot polarization imaging. Second, without any moving mechanical components, this compact camera is well suited for *in-situ* imaging of live animals in studies of neuroethology and sensory ecology [269]. Finally, unlike conventional rotating-polarizer-based imaging polarimetry, the MPA-filtered camera is not affected by temperature-dependent co-registration errors [270], which enhances its measurement accuracy.

Table 1. Comparative summary of representative techniques in single-shot coded-aperture optical imaging.

Category	Encoding approach	Representative technique	Coded aperture's location	Coded aperture's pattern	Coded-aperture's function	Selected application
Planar imaging	Active	TEGI microscopy [61]	Object plane	Temporally coded grayscale pattern	Production of PSFs with flat Fourier spectra	Motion deblurring in microscopy [61]
	Passive	CRSP [73]	Sensor plane	Spatiotemporally staggered pattern	Spatiotemporal sampling	High dynamic range photography [73]
Depth imaging	Active	Microsoft Kinect™ [118, 119]	Object plane	Random dot-array pattern	Production of codewords for grid-index matching	Human-computer interaction [126]
	Passive	FlatScope [134, 135]	Between object and sensor	MURA pattern	Production of depth-dependent PSFs	3D fluorescence microscopy [135]
Light-field imaging	Active	LF-BOS photography [148]	Object plane	Color-intensity gradient pattern	Mapping light field to color and intensity	Schlieren photography of transparent objects [148]
	Passive	HLF camera [153]	Between object and sensor	Summation of 2D cosine harmonics	Light-field multiplexing	Digital refocusing [153]
Temporal imaging	Active	STAMP [177]	Object plane pattern	Uniform binary	Mapping spectrum to time	Light-matter interaction [177]
	Passive	CUP [185]	Between object and sensor	Random binary pattern	Compressive sampling	Light dynamics visualization [196, 197]
Spectral imaging	Active	FSM device [226]	Object plane	2D sinusoidal patterns	Spatiospectral multiplexing	Analysis of diffusion process [226]
	Passive	HPA™ camera [238]	Between object and sensor	Pinhole array	Spatiospectral sampling	Chemical detection and analysis [239]
Polarization imaging	Active	RPM [258]	Object plane	Annular ring	Mapping polarization to color and intensity	Analysis of birefringence in biological samples [258]
	Passive	MPA-filtered CCD camera [248]	Sensor plane	Four-value MPA	Spatio-polarization filtering	Marine biology [268]

8. Conclusions and outlook

In this review, we present a taxonomy of single-shot coded-aperture optical imaging, arranged according to the measured photon tags. The field can be divided into six categories—planar imaging, depth imaging, light-field imaging, temporal imaging, spectral imaging, and polarization imaging. According to the position of the coded aperture with respect to the scene, these categories are further divided into active-encoding and the passive-encoding approaches. A total of 12 representative techniques are surveyed from the aspects of system schematics, data acquisition, image reconstruction, and selected applications, as well as their advantages and/or limitations. This information is summarized in table 1. The examples presented were not selected for the popularity of the techniques, but rather to broadly cover typical functions of coded apertures used in imaging systems. In addition, to promote interaction between related communities, six techniques were selected from the literature in computer graphics, while the other six were chosen from publications in optics. Of course, coded aperture techniques are not limited to these examples. Several popular techniques in each category are also been briefly mentioned at the beginning of each section in sections 2–7. However, a fully panoramic view of this fast-expanding field is never possible, resulting in possible omissions. Therefore, this review serves as a pedagogical tool to provide researchers with deeper insights into typical methods and applications of single-shot coded-aperture optical imaging. In practice, researchers could use these general guidelines to develop the most suitable technique for their specific studies.

Single-shot coded-aperture optical imaging will certainly continue its fast growth. This interdisciplinary field is built upon the marriage of optical engineering and computer science. Fast progress in related disciplines, such as optoelectronic devices, lasers, and imaging sciences, as well as computational power, advanced algorithms, and signal processing theories, will create new imaging techniques and will improve the performance of existing ones. Both disciplinary advances, in turn, will enable new applications in both science and industry. In the following, we provide an outlook on potential technical development.

First, the synergy of a coded aperture with optical components that perform the shearing operation could become a general design concept in single-shot coded-aperture optical imaging. The shearing operation is naturally embedded in many optical processes. For example, shearing is incorporated in the model to describe image blurring [61] (section 2). Light propagation automatically induces shearing in phase-space measurement for light-field imaging [39] (section 4). Temporal shearing can be readily performed by using various streak cameras [164, 172] (section 5). Spectral

shearing is routinely achieved using standard optical components, such as prisms and gratings (section 6). In addition, shearing is an elegant way to reduce the dimensions of datacubes for use within the 2D (i.e. x, y) imaging capability of standard cameras. The prior information provided by the coded aperture will allow unmixing the multiplexed measurement. Among the six categories, four have implemented coded apertures with a shearing operation. It is expected that this paradigm will soon be adapted to sense depth and polarization in single-shot coded-aperture optical imaging.

Second, high-dimensional single-shot coded-aperture optical imaging will gain increasing research attention. Many optical events are reflected simultaneously by multiple photon tags, and its high-dimensional imaging capability will significantly enhance the application scope of single-shot coded-aperture optical imaging. Thus far, a few techniques have already been explored, including coded-aperture snapshot spectral polarization imaging [271] and compressive spectral temporal imaging [205, 272]. It is envisaged that coded apertures could provide a path that leads to single-shot optical imaging with all the photon tags covered in this review.

Third, the interaction of different fields and the exchange of existing techniques in single-shot coded-aperture optical imaging will be increasingly promoted. The underlying mathematical expressions of many single-shot coded-aperture imaging techniques are universal and can thus be adapted to other systems. Examples include CUP (section 5.2) and CASSI, as well as the FRAME technique and the FSM device (section 6.1). It is also predicted that these advances in optics will spur conventional coded-aperture imaging using high-energy radiation.

Fourth, deep-learning-based computational frameworks will be progressively used in single-shot coded-aperture optical imaging. Artificial intelligence could partially compensate for the incapabilities of existing physical-model-based reconstruction algorithms. Therefore, its adoption in this field is a natural and fruitful research direction. Recent research has successfully implemented the deep neural network in sensing depth and spectrum in single-shot coded-aperture optical imaging [273, 274]. This trend will undoubtedly continue and diffuse into other categories in this field. In addition, artificial intelligence could assist in optimizing coded apertures. Many established theories are applicable to refining the patterns on the coded apertures, including the restricted isometry property [192] and image noise models [275]. The implementation of novel algorithms in aperture optimization will continue to be an integral part of the research.

Acknowledgments

The author thanks Prof James Ballard for editing the manuscript. This work is supported by Natural Sciences and Engineering Research Council (NSERC) of Canada (RGPIN-2017-05959, RGPAS-507845-2017, CRDPJ-532304-18, ALLRP-549833-2020), Fonds de recherche du Québec–Nature et technologies (FRQNT) (2019-NC-252960), and Fonds de recherche du Québec–Santé (FRQS) (280229, 267406).

ORCID iDs

Jinyang Liang https://orcid.org/0000-0001-5983-0488

References

[1] Šiaulys N, Gallais L and Melninkaitis A 2014 Direct holographic imaging of ultrafast laser damage process in thin films *Opt. Lett.* **39** 2164–7
[2] Poulin P R and Nelson K A 2006 Irreversible organic crystalline chemistry monitored in real time *Science* **313** 1756–60
[3] Gong Y, Huang C, Li J Z, Grewe B F, Zhang Y, Eismann S and Schnitzer M J 2015 High-speed recording of neural spikes in awake mice and flies with a fluorescent voltage sensor *Science* **350** 1361–6
[4] Liang J and Wang L V 2018 Single-shot ultrafast optical imaging *Optica* **5** 1113–27
[5] Bradley D K, Bell P M, Kilkenny J D, Hanks R, Landen O, Jaanimagi P A, McKenty P W and Verdon C P 1992 High-speed gated x-ray imaging for ICF target experiments (invited) *Rev. Sci. Instrum.* **63** 4813–7
[6] Kodama R *et al* 2001 Fast heating of ultrahigh-density plasma as a step towards laser fusion ignition *Nature* **412** 798
[7] Li Z *et al* 2016 Single-shot visualization of evolving plasma wakefields *AIP Conf. Proc.* **1777** 040010
[8] Zhang Z H 2012 Review of single-shot 3D shape measurement by phase calculation-based fringe projection techniques *Opt. Lasers Eng.* **50** 1097–106
[9] Descour M and Dereniak E 1995 Computed-tomography imaging spectrometer: experimental calibration and reconstruction results *Appl. Opt.* **34** 4817–26
[10] Hagen N *et al* 2012 Snapshot advantage: a review of the light collection improvement for parallel high-dimensional measurement systems *Opt. Eng.* **51** 111702
[11] The Laser Institute of America 2014 *ANSI Z136.1 Safe Use of Lasers*
[12] Gao L, Bedard N, Hagen N, Kester R T and Tkaczyk T S 2011 Depth-resolved image mapping spectrometer (IMS) with structured illumination *Opt. Express* **19** 17439–52
[13] Hagen N and Kudenov M W 2013 Review of snapshot spectral imaging technologies *Opt. Eng.* **52** 090901
[14] Cannon T and Fenimore E 1980 Coded aperture imaging: many holes make light work *Opt. Eng.* **19** 193283
[15] Chi W and George N 2011 Optical imaging with phase-coded aperture *Opt. Express* **19** 4294–300
[16] Byard K 2012 Index class apertures-a class of flexible coded aperture *Appl. Opt.* **51** 3453–60
[17] Ding J, Noshad M and Tarokh V 2016 Complementary lattice arrays for coded aperture imaging *J. Opt. Soc. Am.* A **33** 863–81
[18] Busboom A, Schotten H D and Elders-Boll H 1997 Coded aperture imaging with multiple measurements *J. Opt. Soc. Am.* A **14** 1058–65
[19] Wang Z and Guo W 2018 Coded pinhole lens imaging *OSA Continuum* **1** 64–77
[20] Oh W Y, Yun S H, Vakoc B J, Shishkov M, Desjardins A E, Park B H, de Boer J F, Tearney G J and Bouma B E 2008 High-speed polarization sensitive optical frequency domain imaging with frequency multiplexing *Opt. Express* **16** 1096–103
[21] Willett R M, Marcia R F and Nichols J M 2011 Compressed sensing for practical optical imaging systems: a tutorial *Opt. Eng.* **50** 072601

[22] Alonso M A 2011 Wigner functions in optics: describing beams as ray bundles and pulses as particle ensembles *Adv. Opt. Photon.* **3** 272–365

[23] Mait J N, Euliss G W and Athale R A 2018 Computational imaging *Adv. Opt. Photon.* **10** 409–83

[24] Gao L and Wang L V 2016 A review of snapshot multidimensional optical imaging: measuring photon tags in parallel *Phys. Rep.* **616** 1–37

[25] Wetzstein G *et al* 2011 Computational plenoptic imaging *Computer Graphics Forum* (New York: Wiley)

[26] Zhu S, Gao L, Zhang Y, Lin J and Jin P 2018 Complete plenoptic imaging using a single detector *Opt. Express* **26** 26495–510

[27] Caroli E *et al* 1987 Coded aperture imaging in x- and gamma-ray astronomy *Space Sci. Rev.* **45** 349–403

[28] Hirschfeld T 1976 Fellgett's advantage in UV–VIS multiplex spectroscopy *Appl. Spectrosc.* **30** 68–9

[29] Chen Z, Liu B, Wang S and Liu E 2018 Polarization-modulated three-dimensional imaging using a large-aperture electro-optic modulator *Appl. Opt.* **57** 7750–7

[30] Liang J, Wu S-Y, Kohn R N, Becker M F and Heinzen D J 2012 Grayscale laser image formation using a programmable binary mask *Opt. Eng.* **51** 108201

[31] Bagnoud V and Zuegel J D 2004 Independent phase and amplitude control of a laser beam by use of a single-phase-only spatial light modulator *Opt. Lett.* **29** 295–7

[32] Liang J and Becker M F 2014 Spatial bandwidth analysis of fast backward Fresnel diffraction for precise computer-generated hologram design *Appl. Opt.* **53** G84–94

[33] Barrett H H and Horrigan F A 1973 Fresnel zone plate imaging of gamma rays; theory *Appl. Opt.* **12** 2686–702

[34] Fenimore E E and Cannon T M 1978 Coded aperture imaging with uniformly redundant arrays *Appl. Opt.* **17** 337–47

[35] Chen Y-W and Kishimoto K 2003 Tomographic resolution of uniformly redundant arrays coded aperture *Rev. Sci. Instrum.* **74** 2232–5

[36] Shutler P M E, Springham S V and Talebitaher A 2013 Mask design and fabrication in coded aperture imaging *Nucl. Instrum. Methods Phys. Res.* A **709** 129–42

[37] Waller L and Tian L 2015 Machine learning for 3D microscopy *Nature* **523** 416

[38] Cieślak M J, Gamage K A and Glover R 2016 Coded-aperture imaging systems: past, present and future development–a review *Radiat. Meas.* **92** 59–71

[39] Zhou C and Nayar S K 2011 Computational cameras: convergence of optics and processing *IEEE Trans. Image Process.* **20** 3322–40

[40] NASA 2020 Coded aperture imaging in high-energy astronomy (https://asd.gsfc.nasa.gov/archive/cai/coded.html) (Accessed: 5th July 2020)

[41] Van der Jeught S and Dirckx J J J 2016 Real-time structured light profilometry: a review *Opt. Lasers Eng.* **87** 18–31

[42] Jiang C, Kilcullen P, Liu X, Gribben J, Boate A, Ozaki T and Liang J 2020 Real-time high-speed three-dimensional surface imaging using band-limited illumination profilometry with a CoaXpress interface *Opt. Lett.* **45** 964–7

[43] Duarte M F, Davenport M A, Takhar D, Laska J N, Sun T, Kelly K F and Baraniuk R G 2008 Single-pixel imaging via compressive sampling *IEEE Signal Process. Mag.* **25** 83–91

[44] Liang J, Gao L, Li C and Wang L V 2014 Spatially Fourier-encoded photoacoustic microscopy using a digital micromirror device *Opt. Lett.* **39** 430–3

[45] Yang C *et al* 2018 Compressed ultrafast photography by multi-encoding imaging *Laser Phys. Lett.* **15** 116202

[46] Arce G R *et al* 2013 Compressive coded aperture spectral imaging: an introduction *IEEE Signal Process. Mag.* **31** 105–15

[47] Zuo C, Sun J, Feng S, Zhang M and Chen Q 2016 Programmable aperture microscopy: a computational method for multi-modal phase contrast and light field imaging *Opt. Lasers Eng.* **80** 24–31

[48] Luo W, Greenbaum A, Zhang Y and Ozcan A 2015 Synthetic aperture-based on-chip microscopy *Light Sci. Appl.* **4** e261

[49] Egan W G, Johnson W R and Whitehead V S 1991 Terrestrial polarization imagery obtained from the space shuttle: characterization and interpretation *Appl. Opt.* **30** 435–42

[50] Teng J *et al* 2019 Time-encoded single-pixel 3D imaging (arXiv:1901.04141)

[51] Lam E Y 2015 Computational photography with plenoptic camera and light field capture: tutorial *J. Opt. Soc. Am.* A **32** 2021–32

[52] Chan S C 2014 Plenoptic function *Computer Vision: A Reference Guide* ed K Ikeuchi (Berlin: Springer) pp 618–23

[53] Welford W T 1960 Use of annular apertures to increase focal depth *J. Opt. Soc. Am.* **50** 749–53

[54] Ojeda-Castañeda J, Andrés P and Díaz A 1986 Annular apodizers for low sensitivity to defocus and to spherical aberration *Opt. Lett.* **11** 487–9

[55] Ben-Ezra M, Lin Z and Wilburn B 2007 Penrose pixels super-resolution in the detector layout domain *2007 IEEE 11th Int. Conf. on Computer Vision* (Piscataway, NJ: IEEE)

[56] Asif M S *et al* 2016 Flatcam: thin, lensless cameras using coded aperture and computation *IEEE Trans. Comput. Imaging* **3** 384–97

[57] Katz O, Heidmann P, Fink M and Gigan S 2014 Non-invasive single-shot imaging through scattering layers and around corners via speckle correlations *Nat. Photon.* **8** 784–90

[58] Chung J, Martinez G W, Lencioni K C, Sadda S R and Yang C 2019 Computational aberration compensation by coded-aperture-based correction of aberration obtained from optical Fourier coding and blur estimation *Optica* **6** 647–61

[59] Pueo B 2016 High speed cameras for motion analysis in sports science *J. Hum. Sport Exerc.* **11** 53–73

[60] Agrawal A 2020 License plate from blurred photo taken with a 'Flutter Shutter Camera' (http://www.cs.cmu.edu/~ILIM/projects/IM/aagrawal/sig06/license.html) (Accessed: 5th July 2020)

[61] Ma C, Liu Z, Tian L, Dai Q and Waller L 2015 Motion deblurring with temporally coded illumination in an LED array microscope *Opt. Lett.* **40** 2281–4

[62] Raskar R, Agrawal A and Tumblin J 2006 Coded exposure photography: motion deblurring using fluttered shutter *ACM Trans. Graph.* (New York: ACM)

[63] Gorthi S S, Schaak D and Schonbrun E 2013 Fluorescence imaging of flowing cells using a temporally coded excitation *Opt. Express* **21** 5164–70

[64] Richardson W H 1972 Bayesian-based iterative method of image restoration* *J. Opt. Soc. Am.* **62** 55–9

[65] Lucy L B 1974 An iterative technique for the rectification of observed distributions *Astrophys. J.* **79** 745

[66] McCloskey S 2011 Temporally coded flash illumination for motion deblurring *2011 Int. Conf. on Computer Vision* (Piscataway, NJ: IEEE)

[67] Tendero Y and Osher S 2016 On a mathematical theory of coded exposure *Res. Math. Sci.* **3** 4

[68] Agrawal A and Xu Y 2009 Coded exposure deblurring: optimized codes for PSF estimation and invertibility *2009 IEEE Conf. on Computer Vision and Pattern Recognition* (Piscataway, NJ: IEEE)

[69] Park K *et al* 2014 Motion deblurring using coded exposure for a wheeled mobile robot *2014 11th Int. Conf. on Ubiquitous Robots and Ambient Intelligence (URAI)* (Piscataway, NJ: IEEE)

[70] Yitzhaky Y, Mor I, Lantzman A and Kopeika N S 1998 Direct method for restoration of motion-blurred images *J. Opt. Soc. Am.* A **15** 1512–9

[71] Kundur D and Hatzinakos D 1998 A novel blind deconvolution scheme for image restoration using recursive filtering *IEEE Trans. Signal Process.* **46** 375–90

[72] Tull D L and Katsaggelos A K 1996 Iterative restoration of fast-moving objects in dynamic image sequences *Opt. Eng.* **35** 3460

[73] Gu J *et al* 2010 Coded rolling shutter photography: flexible space-time sampling *2010 IEEE Int. Conf. on Computational Photography (ICCP)* (Piscataway, NJ: IEEE)

[74] Ait-Aider O, Bartoli A and Andreff N 2007 Kinematics from lines in a single rolling shutter image *2007 IEEE Conf. on Computer Vision and Pattern Recognition* (Piscataway, NJ: IEEE)

[75] Baker S, Scharstein D, Lewis J P, Roth S, Black M J and Szeliski R 2011 A database and evaluation methodology for optical flow *Int. J. Comput. Vis.* **92** 1–31

[76] Keller S H, Lauze F and Nielsen M 2008 Deinterlacing using variational methods *IEEE Trans. Image Process.* **17** 2015–28

[77] De Haan G and Bellers E B 1998 Deinterlacing-an overview *Proc. IEEE* **86** 1839–57

[78] Kwon O, Sohn K and Lee C 2003 Deinterlacing using directional interpolation and motion compensation *IEEE Trans. Consum. Electron.* **49** 198–203

[79] Debevec P E and Malik J 2008 Recovering high dynamic range radiance maps from photographs *ACM SIGGRAPH 2008 Classes* (New York: ACM)

[80] Mitsunaga T and Nayar S K 1999 Radiometric self calibration *Proc. 1999 IEEE Computer Society Conf. on Computer Vision and Pattern Recognition (Cat. No PR00149)* (Piscataway, NJ: IEEE)

[81] Fossum E R 1997 CMOS image sensors: electronic camera-on-a-chip *IEEE Trans. Electron Devices* **44** 1689–98

[82] Nakamura J 2016 *Image Sensors and Signal Processing for Digital Still Cameras* (Boca Raton, FL: CRC Press)

[83] Nayar S K and Mitsunaga T 2000 High dynamic range imaging: spatially varying pixel exposures *Proc. IEEE Conf. on Computer Vision and Pattern Recognition CVPR 2000 (Cat. No. PR00662)* (Piscataway, NJ: IEEE)

[84] Sukumar S R *et al* 2006 Robotic three-dimensional imaging system for under-vehicle inspection *J. Electron. Imaging* **15** 033008

[85] Zennaro S *et al* 2015 Performance evaluation of the 1st and 2nd generation Kinect for multimedia applications *2015 IEEE Int. Conf. on Multimedia and Expo (ICME)* (Piscataway, NJ: IEEE)

[86] Maier-Hein L *et al* 2014 Comparative validation of single-shot optical techniques for laparoscopic 3D surface reconstruction *IEEE Trans. Med. Imaging* **33** 1913–30

[87] Palacios J, Sagüés C, Montijano E and Llorente S 2013 Human-computer interaction based on hand gestures using RGB-D sensors *Sensors* **13** 11842–60

[88] Foix S, Alenya G and Torras C 2011 Lock-in time-of-flight (ToF) cameras: a survey *IEEE Sens. J.* **11** 1917–26

[89] Kolb A *et al* 2010 Time-of-flight cameras in computer graphics *Computer Graphics Forum* (New York: Wiley)

[90] Geng J 2011 Structured-light 3D surface imaging: a tutorial *Adv. Opt. Photon.* **3** 128–60

[91] Zuo C, Tao T, Feng S, Huang L, Asundi A and Chen Q 2018 Micro Fourier transform profilometry (μFTP): 3D shape measurement at 10 000 frames per second *Opt. Lasers Eng.* **102** 70–91

[92] Zhou C, Liu T, Si S, Xu J, Liu Y and Lei Z 2015 An improved stair phase encoding method for absolute phase retrieval *Opt. Lasers Eng.* **66** 269–78

[93] Geng Z J 1996 Rainbow three-dimensional camera: new concept of high-speed three-dimensional vision systems *Opt. Eng.* **35** 376–84

[94] Liu W, Wang Z, Mu G and Fang Z 2000 Color-coded projection grating method for shape measurement with a single exposure *Appl. Opt.* **39** 3504–8

[95] Dai M, Yang F and He X 2012 Single-shot color fringe projection for three-dimensional shape measurement of objects with discontinuities *Appl. Opt.* **51** 2062–9

[96] MacWilliams F J and Sloane N J A 1976 Pseudo-random sequences and arrays *Proc. IEEE* **64** 1715–29

[97] Payeur P and Desjardins D 2009 Structured light stereoscopic imaging with dynamic pseudo-random patterns *Int. Conf. Image Analysis and Recognition* (Berlin: Springer)

[98] Griffin P M, Narasimhan L S and Yee S R 1992 Generation of uniquely encoded light patterns for range data acquisition *Pattern Recognit.* **25** 609–16

[99] Maruyama M and Abe S 1993 Range sensing by projecting multiple slits with random cuts *IEEE Trans. Pattern Anal. Mach. Intell.* **15** 647–51

[100] Durdle N G, Thayyoor J and Raso V 1998 An improved structured light technique for surface reconstruction of the human trunk *Conf. Proc. IEEE Canadian Conf. on Electrical and Computer Engineering (Cat. No. 98TH8341)* (Piscataway, NJ: IEEE)

[101] Wang Z and Yang Y 2018 Single-shot three-dimensional reconstruction based on structured light line pattern *Opt. Lasers Eng.* **106** 10–6

[102] Li B, An Y and Zhang S 2016 Single-shot absolute 3D shape measurement with Fourier transform profilometry *Appl. Opt.* **55** 5219–25

[103] Zhong J and Weng J 2004 Spatial carrier-fringe pattern analysis by means of wavelet transform: wavelet transform profilometry *Appl. Opt.* **43** 4993–8

[104] Gdeisat M A, Abid A, Burton D R, Lalor M J, Lilley F, Moore C and Qudeisat M 2009 Spatial and temporal carrier fringe pattern demodulation using the one-dimensional continuous wavelet transform: recent progress, challenges, and suggested developments *Opt. Lasers Eng.* **47** 1348–61

[105] Lu M, Su X, Cao Y, You Z and Zhong M 2016 Modulation measuring profilometry with cross grating projection and single shot for dynamic 3D shape measurement *Opt. Lasers Eng.* **87** 103–10

[106] Antipa N, Kuo G, Heckel R, Mildenhall B, Bostan E, Ng R and Waller L 2018 DiffuserCam: lensless single-exposure 3D imaging *Optica* **5** 1–9

[107] Rai M R, Vijayakumar A and Rosen J 2017 Single camera shot interferenceless coded aperture correlation holography *Opt. Lett.* **42** 3992–5

[108] Lew M D, Lee S F, Ptacin J L, Lee M K, Twieg R J, Shapiro L and Moerner W E 2011 Three-dimensional superresolution colocalization of intracellular protein superstructures and the cell surface in live Caulobacter crescentus *Proc. Natl Acad. Sci.* **108** E1102–10

[109] Jia S, Vaughan J C and Zhuang X 2014 Isotropic three-dimensional super-resolution imaging with a self-bending point spread function *Nat. Photon.* **8** 302–6

[110] Vijayakumar A *et al* 2018 Coded aperture correlation holography system for recording secured digital holograms of incoherently illuminated 3D scenes *Advanced Secure Optical Image Processing for Communications* (Bristol: IOP Publishing) ch 4

[111] Shin J, Tran D N, Stroud J R, Chin S, Tran T D and Foster M A 2019 A minimally invasive lens-free computational microendoscope *Sci. Adv.* **5** eaaw5595

[112] Levin A, Fergus R, Durand F and Freeman W T 2007 Image and depth from a conventional camera with a coded aperture *ACM Trans. Graph.* **26** 70

[113] Subbarao M 1988 Parallel depth recovery by changing camera parameters *ICCV*

[114] Schechner Y Y and Kiryati N 2000 Depth from defocus vs stereo: How different really are they? *Int. J. Comput. Vis.* **39** 141–62

[115] Watanabe M and Nayar S K 1998 Rational filters for passive depth from defocus *Int. J. Comput. Vis.* **27** 203–25

[116] Chi W, Chu K and George N 2006 Polarization coded aperture *Opt. Express* **14** 6634–42

[117] Bando Y, Chen B-Y and Nishita T 2008 Extracting depth and matte using a color-filtered aperture *ACM Trans. Graph.* (New York: ACM)

[118] Naeemabadi M, Dinesen B, Andersen O K and Hansen J 2018 Investigating the impact of a motion capture system on Microsoft Kinect v2 recordings: a caution for using the technologies together *PloS one* **13** e0204052

[119] Dal Mutto C, Zanuttigh P and Cortelazzo G M 2012 Microsoft Kinect^{TM} range camera *Time-of-Flight Cameras and Microsoft Kinect^{TM}* (Berlin: Springer) pp 33–47

[120] Freedman B *et al* 2012 Depth mapping using projected patterns *Google Patents* U.S. Patent 8 150 142

[121] Smisek J, Jancosek M and Pajdla T 2013 3D with Kinect *Consumer Depth Cameras for Computer Vision* (Berlin: Springer) pp 3–25

[122] Konolige K and Mihelich P 2011 Technical description of Kinect calibration

[123] Szeliski R 2010 *Computer Vision: Algorithms and Applications* (Berlin: Springer)

[124] Scharstein D and Szeliski R 2002 A taxonomy and evaluation of dense two-frame stereo correspondence algorithms *Int. J. Comput. Vis.* **47** 7–42

[125] Sarbolandi H, Lefloch D and Kolb A 2015 Kinect range sensing: structured-light versus time-of-flight Kinect *Comput. Vis. Image Underst.* **139** 1–20

[126] Gallo L, Placitelli A P and Ciampi M 2011 Controller-free exploration of medical image data: experiencing the Kinect *2011 24th Int. Symp. on Computer-Based Medical Systems (CBMS)* (Piscataway, NJ: IEEE)

[127] El-laithy R A, Huang J and Yeh M 2012 Study on the use of Microsoft Kinect for robotics applications *Proc. 2012 IEEE/ION Position, Location and Navigation Symp.* (Piscataway, NJ: IEEE)

[128] Gonzalez-Jorge H, Rodríguez-Gonzálvez P, Martínez-Sánchez J, González-Aguilera D, Arias P, Gesto M and Díaz-Vilariño L 2015 Metrological comparison between Kinect I and Kinect II sensors *Measurement* **70** 21–6

[129] Vera L *et al* 2011 Augmented mirror: interactive augmented reality system based on kinect *IFIP Conf. on Human-Computer Interaction* (Berlin: Springer)

[130] Azzari G, Goulden M and Rusu R 2013 Rapid characterization of vegetation structure with a Microsoft Kinect sensor *Sensors* **13** 2384–98

[131] Caon M *et al* 2011 Context-aware 3D gesture interaction based on multiple Kinects *Proc. 1st Int. Conf. on Ambient Computing, Applications, Services and Technologies, AMBIENT* (Citeseer)

[132] Oliver M, Montero F, Molina J P, González P and Fernández-Caballero A 2016 Multi-camera systems for rehabilitation therapies: a study of the precision of Microsoft Kinect sensors *Frontiers Inf. Technol. Electron. Eng.* **17** 348–64

[133] Haggag H *et al* 2013 Measuring depth accuracy in RGBD cameras *7th Int. Conf. on Signal Processing and Communication Systems (ICSPCS)* (Piscataway, NJ: IEEE)

[134] Asif M S, Ayremlou A, Sankaranarayanan A, Veeraraghavan A and Baraniuk R G 2017 FlatCam: thin, lensless cameras using coded aperture and computation *IEEE Trans. Comput. Imaging* **3** 384–97

[135] Adams J K, Boominathan V, Avants B W, Vercosa D G, Ye F, Baraniuk R G, Robinson J T and Veeraraghavan A 2017 Single-frame 3D fluorescence microscopy with ultraminiature lensless FlatScope *Sci. Adv.* **3** e1701548

[136] Gottesman S R and Fenimore E E 1989 New family of binary arrays for coded aperture imaging *Appl. Opt.* **28** 4344–52

[137] Beck A and Teboulle M 2009 A fast iterative shrinkage-thresholding algorithm for linear inverse problems *SIAM J. Imaging Sci.* **2** 183–202

[138] Levoy M and Hanrahan P 1996 Light field rendering *Proc. 23rd Annual Conf. on Computer Graphics and Interactive Techniques*

[139] Ng R 2006 *Digital Light Field Photography* (Stanford, CA: Stanford University)

[140] Ando T, Horisaki R, Nakamura T and Tanida J 2015 Single-shot acquisition of optical direct and global components using single coded pattern projection *Japan J. Appl. Phys.* **54** 042501

[141] Wetzstein G *et al* 2012 Tensor displays: compressive light field synthesis using multilayer displays with directional backlighting *ACM Trans. Graph.* **31** 80

[142] Sidorenko P and Cohen O 2016 Single-shot ptychography *Optica* **3** 9–14

[143] Zhu Z *et al* 2019 Single-shot direct tomography of the complete transverse amplitude, phase, and polarization structure of a light field *Phys. Rev. Appl.* **12** 034036

[144] Marwah K *et al* 2013 Compressive light field photography using overcomplete dictionaries and optimized projections *ACM Trans. Graph.* **32** 46

[145] Antipa N *et al* 2016 Single-shot diffuser-encoded light field imaging *2016 IEEE Int. Conf. on Computational Photography (ICCP)* (Piscataway, NJ: IEEE)

[146] Xu Z, Ke J and Lam E Y 2012 High-resolution lightfield photography using two masks *Opt. Express* **20** 10971–83

[147] Greengard A, Schechner Y Y and Piestun R 2006 Depth from diffracted rotation *Opt. Lett.* **31** 181–3

[148] Wetzstein G, Heidrich W and Raskar R 2014 Computational Schlieren photography with light field probes *Int. J. Comput. Vis.* **110** 113–27

[149] Wetzstein G *et al* 2011 Refractive shape from light field distortion *2011 Int. Conf. on Computer Vision* (Piscataway, NJ: IEEE)

[150] Dalziel S B, Hughes G O and Sutherland B R 2000 Whole-field density measurements by 'synthetic Schlieren' *Exp. Fluids* **28** 322–35

[151] Arpa A *et al* 2012 Single lens off-chip cellphone microscopy *2012 IEEE Computer Society Conf. on Computer Vision and Pattern Recognition Workshops* (Piscataway, NJ: IEEE)

[152] Wetzstein G *et al* 2012 *Tensor Displays: Compressive Light Field Synthesis Using Multilayer Displays with Directional Backlighting ACM Trans. Graph.* **31** 80

[153] Veeraraghavan A *et al* 2007 Dappled photography: mask enhanced cameras for heterodyned light fields and coded aperture refocusing *ACM Trans. Graph.* (New York: ACM)

[154] Wang S and Heidrich W 2004 The design of an inexpensive very high resolution scan camera system *Computer Graphics Forum* (New York: Wiley)

[155] Ng R 2005 Fourier slice photography *ACM Trans. Graph.* (New York: ACM)

[156] Ng R *et al* 2005 Light field photography with a hand-held plenoptic camera *Comput. Sci. Tech. Rep.* **2** 1–11

[157] Levoy M, Ng R, Adams A, Footer M and Horowitz M 2006 Light field microscopy *ACM Trans. Graph.* **25** 924–34

[158] Raskar R *et al* 2008 Glare aware photography: 4D ray sampling for reducing glare effects of camera lenses *ACM Trans. Graph.* **27** 56

[159] Fermann M E, Galvanauskas A and Sucha G 2002 *Ultrafast Lasers: Technology and Applications* vol 80 (Boca Raton, FL: CRC Press)

[160] Patwardhan S V and Culver J P 2008 Quantitative diffuse optical tomography for small animals using an ultrafast gated image intensifier *J. Biomed. Opt.* **13** 011009

[161] Kirmani A, Venkatraman D, Shin D, Colaço A, Wong F N C, Shapiro J H and Goyal V K 2014 First-photon imaging *Science* **343** 58–61

[162] Ishikawa H 2008 *Ultrafast All-Optical Signal Processing Devices* (New York: Wiley)

[163] El-Desouki M, Jamal Deen M, Fang Q, Liu L, Tse F and Armstrong D 2009 CMOS image sensors for high speed applications *Sensors* **9** 430–44

[164] Hamamatsu K K 2020 Guide to streak cameras (https://www.hamamatsu.com/resources/pdf/sys/SHSS0006E_STREAK.pdf) (Accessed: 5th July 2020)

[165] Nayar S K 2006 Computational cameras: redefining the image *Computer* **39** 30–8

[166] Hu X-m, Wu J-m, Suo J-l and Dai Q-h 2017 Emerging theories and technologies on computational imaging *Frontiers Inf. Technol. Electron. Eng.* **18** 1207–21

[167] Faccio D and Velten A 2018 A trillion frames per second: the techniques and applications of light-in-flight photography *Rep. Prog. Phys.* **81** 105901

[168] Sidorenko P, Lahav O and Cohen O 2017 Ptychographic ultrahigh-speed imaging *Opt. Express* **25** 10997–1008

[169] Wengrowicz O, Peleg O, Loevsky B, Chen B K, Haham G I, Sainadh U S and Cohen O 2019 Experimental time-resolved imaging by multiplexed ptychography *Opt. Express* **27** 24568–77

[170] Ehn A, Bood J, Li Z, Berrocal E, Aldén M and Kristensson E 2017 FRAME: femtosecond videography for atomic and molecular dynamics *Light Sci. Appl.* **6** e17045

[171] Yue Q-Y, Cheng Z-J, Han L, Yang Y and Guo C-S 2017 One-shot time-resolved holographic polarization microscopy for imaging laser-induced ultrafast phenomena *Opt. Express* **25** 14182–91

[172] Liu X, Liu J, Jiang C, Vetrone F and Liang J 2019 Single-shot compressed optical-streaking ultra-high-speed photography *Opt. Lett.* **44** 1387–90

[173] Luo Y, Jiang J, Cai M and Mirabbasi S 2019 CMOS computational camera with a two-tap coded exposure image sensor for single-shot spatial-temporal compressive sensing *Opt. Express* **27** 31475–89

[174] Mochizuki F, Kagawa K, Okihara S-i, Seo M-W, Zhang B, Takasawa T, Yasutomi K and Kawahito S 2016 Single-event transient imaging with an ultra-high-speed temporally compressive multi-aperture CMOS image sensor *Opt. Express* **24** 4155–76

[175] Koller R, Schmid L, Matsuda N, Niederberger T, Spinoulas L, Cossairt O, Schuster G and Katsaggelos A K 2015 High spatio-temporal resolution video with compressed sensing *Opt. Express* **23** 15992–6007

[176] Llull P, Liao X, Yuan X, Yang J, Kittle D, Carin L, Sapiro G and Brady D J 2013 Coded aperture compressive temporal imaging *Opt. Express* **21** 10526–45

[177] Nakagawa K *et al* 2014 Sequentially timed all-optical mapping photography (STAMP) *Nat. Photon.* **8** 695–700

[178] Tamamitsu M, Nakagawa K, Horisaki R, Iwasaki A, Oishi Y, Tsukamoto A, Kannari F, Sakuma I and Goda K 2015 Design for sequentially timed all-optical mapping photography with optimum temporal performance *Opt. Lett.* **40** 633–6

[179] Adachi S, Koehl R M and Nelson K A 2000 Real-space and real-time imaging of polariton wavepackets *J. Lumin.* **87–89** 840–3

[180] Vaughan J C, Hornung T, Stone K W and Nelson K A 2007 Coherently controlled ultrafast four-wave mixing spectroscopy *J. Phys. Chem.* A **111** 4873–83

[181] Lee Y-S 2009 *Principles of Terahertz Science and Technology* vol 170 (Berlin: Springer)

[182] Marom D M *et al* 2005 Wavelength-selective 1/spl times/K switches using free-space optics and MEMS micromirrors: theory, design, and implementation *J. Lightwave Technol.* **23** 1620

[183] Okamoto T and Yamaguchi I 1991 Simultaneous acquisition of spectral image information *Opt. Lett.* **16** 1277–9

[184] Pawlowski M E, Dwight J G, Nguyen T-U and Tkaczyk T S 2019 High performance image mapping spectrometer (IMS) for snapshot hyperspectral imaging applications *Opt. Express* **27** 1597–612

[185] Gao L, Liang J, Li C and Wang L V 2014 Single-shot compressed ultrafast photography at one hundred billion frames per second *Nature* **516** 74–7

[186] Candes E J and Wakin M B 2008 An introduction to compressive sampling *IEEE Signal Process. Mag.* **25** 21–30

[187] Hunt J, Driscoll T, Mrozack A, Lipworth G, Reynolds M, Brady D and Smith D R 2013 Metamaterial apertures for computational imaging *Science* **339** 310–3

[188] Bioucas-Dias J M and Figueiredo M A T 2007 A new TwIST: two-step iterative shrinkage/thresholding algorithms for image restoration *IEEE Trans. Image Process.* **16** 2992–3004

[189] Chan S H, Wang X and Elgendy O A 2016 Plug-and-play ADMM for image restoration: fixed-point convergence and applications *IEEE Trans. Comput. Imaging* **3** 84–98

[190] Yang C *et al* 2019 Improving the image reconstruction quality of compressed ultrafast photography via an augmented Lagrangian algorithm *J. Opt.* **21** 035703

[191] Zhu L, Chen Y, Liang J, Xu Q, Gao L, Ma C and Wang L V 2016 Space- and intensity-constrained reconstruction for compressed ultrafast photography *Optica* **3** 694–7

[192] Candès E J 2008 The restricted isometry property and its implications for compressed sensing *C. R. Math.* **346** 589–92

[193] Yang C *et al* 2018 Optimizing codes for compressed ultrafast photography by the genetic algorithm *Optica* **5** 147–51

[194] Liu X, Zhang S, Yurtsever A and Liang J 2019 Single-shot real-time sub-nanosecond electron imaging aided by compressed sensing: analytical modeling and simulation *Micron* **117** 47–54

[195] Orović I *et al* 2016 Compressive sensing in signal processing: algorithms and transform domain formulations *Math. Probl. Eng.* **2016** 1–16

[196] Liang J, Zhu L and Wang L V 2018 Single-shot real-time femtosecond imaging of temporal focusing *Light Sci. Appl.* **7** 42

[197] Liang J, Ma C, Zhu L, Chen Y, Gao L and Wang L V 2017 Single-shot real-time video recording of a photonic Mach cone induced by a scattered light pulse *Sci. Adv.* **3** e1601814

[198] Liang J *et al* 2015 Encrypted three-dimensional dynamic imaging using snapshot time-of-flight compressed ultrafast photography *Sci. Rep.* **5** 15504

[199] Yang C *et al* 2018 Compressed 3D image information and communication security *Adv. Quantum Technol.* **1** 1800034

[200] Thompson J *et al* 2017 High speed fluorescence imaging with compressed ultrafast photography *SPIE BiOS* vol 10076 (SPIE)

[201] Kim T, Liang J, Zhu L and Wang L V 2020 Picosecond-resolution phase-sensitive imaging of transparent objects in a single shot *Sci. Adv.* **6** eaay6200

[202] Yang C *et al* 2020 Hyperspectrally compressed ultrafast photography *Phys. Rev. Lett.* **124** 023902

[203] Qi D *et al* 2018 Compressed ultrafast electron diffraction imaging through electronic encoding *Phys. Rev. Appl.* **10** 054061

[204] Lu Y *et al* 2019 Compressed ultrafast spectral-temporal photography *Phys. Rev. Lett.* **122** 193904

[205] Wang P, Liang J and Wang L V 2020 Single-shot ultrafast imaging attaining 70 trillion frames per second *Nat. Commun.* **11** 2091

[206] Wagadarikar A A, Pitsianis N P, Sun X and Brady D J 2009 Video rate spectral imaging using a coded aperture snapshot spectral imager *Opt. Express* **17** 6368–88

[207] Calin M A, Parasca S V, Savastru D and Manea D 2014 Hyperspectral imaging in the medical field: present and future *Appl. Spectrosc. Rev.* **49** 435–47

[208] Lu G and Fei B 2014 Medical hyperspectral imaging: a review *J. Biomed. Opt.* **19** 010901

[209] Johnson W R, Wilson D W, Fink W, Humayun M and Bearman G 2007 Snapshot hyperspectral imaging in ophthalmology *J. Biomed. Opt.* **12** 014036

[210] Cadd S, Li B, Beveridge P, O′Hare W T, Campbell A and Islam M 2016 A comparison of visible wavelength reflectance hyperspectral imaging and acid black 1 for the detection and identification of blood stained fingerprints *Sci. Justice* **56** 247–55

[211] Sinjab F, Liao Z and Notingher I 2019 Applications of spatial light modulators in Raman spectroscopy *Appl. Spectrosc.* **73** 727–46

[212] Qi J and Shih W-C 2012 Parallel Raman microspectroscopy using programmable multipoint illumination *Opt. Lett.* **37** 1289–91

[213] Cao X *et al* 2011 A prism-mask system for multispectral video acquisition *IEEE Trans. Pattern Anal. Mach. Intell.* **33** 2423–35

[214] Dwight J G and Tkaczyk T S 2017 Lenslet array tunable snapshot imaging spectrometer (LATIS) for hyperspectral fluorescence microscopy *Biomed. Opt. Express* **8** 1950–64

[215] Matsuoka H, Kosai Y, Saito M, Takeyama N and Suto H 2002 Single-cell viability assessment with a novel spectro-imaging system *J. Biotechnol.* **94** 299–308

[216] Lukac R and Plataniotis K N 2005 Color filter arrays: design and performance analysis *IEEE Trans. Consum. Electron.* **51** 1260–7

[217] Nussbaum Hoffer N and Michaeli T 2019 Multispectral reconstruction from reference objects in the scene *Proc. of the IEEE Int. Conf. on Computer Vision Workshops*

[218] Nayar S K and Narasimhan S G 2002 Assorted pixels: multi-sampled imaging with structural models *European Conf. on Computer Vision* (Berlin: Springer)

[219] Wagadarikar A, John R, Willett R and Brady D 2008 Single disperser design for coded aperture snapshot spectral imaging *Appl. Opt.* **47** B44–51

[220] Tsai T-H 2016 *Coding Strategies and Implementations of Compressive Sensing* (Durham, CA: Duke University)

[221] Cao X, Yue T, Lin X, Lin S, Yuan X, Dai Q, Carin L and Brady D J 2016 Computational snapshot multispectral cameras: toward dynamic capture of the spectral world *IEEE Signal Process. Mag.* **33** 95–108

[222] Lim S *et al* 2014 Forensic prescreening system using coded aperture snapshot spectral imager *Multisensor, Multisource Information Fusion: Architectures, Algorithms, and Applications 2014* (International Society for Optics and Photonics)

[223] Takeyama S, Ono S and Kumazawa I 2017 Hyperspectral image restoration by hybrid spatio-spectral total variation *2017 IEEE Int. Conf. on Acoustics, Speech and Signal Processing (ICASSP)* (Piscataway, NJ: IEEE)

[224] Yuan X, Tsai T-H, Zhu R, Llull P, Brady D and Carin L 2015 Compressive hyperspectral imaging with side information *IEEE J. Sel. Top. Signal Process.* **9** 964–76

[225] McCain S T *et al* 2012 Coded-aperture Raman imaging for standoff explosive detection *Chemical, Biological, Radiological, Nuclear, and Explosives (CBRNE) Sensing XIII* (International Society for Optics and Photonics)

[226] Deng C, Hu X, Suo J, Zhang Y, Zhang Z and Dai Q 2018 Snapshot hyperspectral imaging via spectral basis multiplexing in Fourier domain *Opt. Express* **26** 32509–21

[227] Liang J, Kohn R N, Becker M F and Heinzen D J 2012 Homogeneous one-dimensional optical lattice generation using a digital micromirror device-based high-precision beam shaper *J. Micro/Nanolith. MEMS MOEMS* **11** 023002

[228] Lau D L and Arce G R 2001 *Modern Digital Halftoning* (Boca Raton, FL: CRC Press)

[229] Liao X, Li H and Carin L 2014 Generalized alternating projection for weighted-$\ell_{2,1}$ minimization with applications to model-based compressive sensing *SIAM J. Imaging Sci.* **7** 797–823

[230] Park J-I *et al* 2007 Multispectral imaging using multiplexed illumination *2007 IEEE 11th Int. Conf. on Computer Vision* (Piscataway, NJ: IEEE)

[231] Han S *et al* 2010 Fast spectral reflectance recovery using DLP projector *Asian Conf. on Computer Vision* (Berlin: Springer)

[232] Parkkinen J P S, Hallikainen J and Jaaskelainen T 1989 Characteristic spectra of Munsell colors *J. Opt. Soc. Am.* A **6** 318–22

[233] Dorozynska K and Kristensson E 2017 Implementation of a multiplexed structured illumination method to achieve snapshot multispectral imaging *Opt. Express* **25** 17211–26

[234] Weitzel L, Krabbe A, Kroker H, Thatte N, Tacconi-Garman L E, Cameron M and Genzel R 1996 3D: the next generation near-infrared imaging spectrometer *Astron. Astrophys. Suppl. Ser.* **119** 531–46

[235] Kudenov M W and Dereniak E L 2010 Compact snapshot birefringent imaging Fourier transform spectrometer *Imaging Spectrometry XV* (International Society for Optics and Photonics)

[236] Gehm M E, John R, Brady D J, Willett R M and Schulz T J 2007 Single-shot compressive spectral imaging with a dual-disperser architecture *Opt. Express* **15** 14013–27

[237] Gunturk B K, Glotzbach J, Altunbasak Y, Schafer R W and Mersereau R M 2005 Demosaicking: color filter array interpolation *IEEE Signal Process. Mag.* **22** 44–54

[238] Bodkin A *et al* 2009 Snapshot hyperspectral imaging: the hyperpixel array camera *Algorithms and Technologies for Multispectral, Hyperspectral, and Ultraspectral Imagery XV* (International Society for Optics and Photonics)

[239] Bodkin A *et al* 2012 Video-rate chemical identification and visualization with snapshot hyperspectral imaging *Next-Generation Spectroscopic Technologies V* (International Society for Optics and Photonics)

[240] Whitenton E *et al* 2016 Assessing the use of an infrared spectrum hyperpixel array imager to measure temperature during additive and subtractive manufacturing *Thermosense: Thermal Infrared Applications XXXVIII* (International Society for Optics and Photonics)

[241] Boniface A, Gusachenko I, Dholakia K and Gigan S 2019 Rapid broadband characterization of scattering medium using hyperspectral imaging *Optica* **6** 274–9

[242] West M, Grossmann J and Galvan C 2019 *Commercial Snapshot Spectral Imaging: The Art of the Possible* (Report No. MTR180488) The MITRE Corporation https://www.mitre.org/sites/default/files/publications/pr-18-3832-commercial-snapshot-spectral-imaging-art-of-possible.pdf

[243] Hsu P S, Lauriola D, Jiang N, Miller J D, Gord J R and Roy S 2017 Fiber-coupled, UV-SWIR hyperspectral imaging sensor for combustion diagnostics *Appl. Opt.* **56** 6029–34

[244] Oiknine Y, August I and Stern A 2018 Multi-aperture snapshot compressive hyperspectral camera *Opt. Lett.* **43** 5042–5

[245] Lake S P and Barocas V H 2011 Mechanical and structural contribution of non-fibrillar matrix in uniaxial tension: a collagen-agarose co-gel model *Ann. Biomed. Eng.* **39** 1891–903
[246] Goldstein D H 2016 *Polarized Light* (Boca Raton, FL: CRC Press)
[247] Gruev V, Perkins R and York T 2010 CCD polarization imaging sensor with aluminum nanowire optical filters *Opt. Express* **18** 19087–94
[248] Garcia M, Edmiston C, Marinov R, Vail A and Gruev V 2017 Bio-inspired color-polarization imager for real-time *in situ* imaging *Optica* **4** 1263–71
[249] Wicker K and Heintzmann R 2010 Single-shot optical sectioning using polarization-coded structured illumination *J. Opt.* **12** 084010
[250] Jost A and Heintzmann R 2013 Superresolution multidimensional imaging with structured illumination microscopy *Annu. Rev. Mater. Res.* **43** 261–82
[251] Gruev V, Ortu A, Lazarus N, Spiegel J V d and Engheta N 2007 Fabrication of a dual-tier thin film micropolarization array *Opt. Express* **15** 4994–5007
[252] Schonbrun E, Möller G and Di Caprio G 2014 Polarization encoded color camera *Opt. Lett.* **39** 1433–6
[253] Cheng C-J and Chen M-L 2004 Polarization encoding for optical encryption using twisted nematic liquid crystal spatial light modulators *Opt. Commun.* **237** 45–52
[254] Carnicer A and Javidi B 2017 Optical security and authentication using nanoscale and thin-film structures *Adv. Opt. Photon.* **9** 218–56
[255] Chen W, Javidi B and Chen X 2014 Advances in optical security systems *Adv. Opt. Photon.* **6** 120–55
[256] Wang Q, Xiong D, Alfalou A and Brosseau C 2018 Optical image encryption method based on incoherent imaging and polarized light encoding *Opt. Commun.* **415** 56–63
[257] Dubreuil M, Alfalou A and Brosseau C 2012 Robustness against attacks of dual polarization encryption using the Stokes–Mueller formalism *J. Opt.* **14** 094004
[258] Samson E C and Blanca C M 2007 Dynamic contrast enhancement in widefield microscopy using projector-generated illumination patterns *New J. Phys.* **9** 363
[259] Wang Y-Q, Zhang D-X and Chen Z-Y 2004 Pollen histochemistry and pollen: ovule ratios in zingiberaceae *Ann. Bot.* **94** 583–91
[260] Park H K *et al* 2016 Horizontally assembled green InGaN nanorod LEDs: scalable polarized surface emitting LEDs using electric-field assisted assembly *Sci. Rep.* **6** 28312
[261] Matioli E, Brinkley S, Kelchner K M, Hu Y-L, Nakamura S, DenBaars S, Speck J and Weisbuch C 2012 High-brightness polarized light-emitting diodes *Light Sci. Appl.* **1** e22
[262] Marinov R, Cui N, Garcia M, Powell S B and Gruev V 2017 A 4-megapixel cooled CCD division of focal plane polarimeter for celestial imaging *IEEE Sens. J.* **17** 2725–33
[263] Gruev V 2011 Fabrication of a dual-layer aluminum nanowires polarization filter array *Opt. Express* **19** 24361–9
[264] Gao S and Gruev V 2013 Gradient-based interpolation method for division-of-focal-plane polarimeters *Opt. Express* **21** 1137–51
[265] Gao S and Gruev V 2011 Bilinear and bicubic interpolation methods for division of focal plane polarimeters *Opt. Express* **19** 26161–73
[266] York T *et al* 2014 Bioinspired polarization imaging sensors: from circuits and optics to signal processing algorithms and biomedical applications *Proc. IEEE* **102** 1450–69
[267] Charanya T *et al* 2014 Trimodal color-fluorescence-polarization endoscopy aided by a tumor selective molecular probe accurately detects flat lesions in colitis-associated cancer *J. Biomed. Opt.* **19** 126002
[268] York T *et al* 2014 Real-time high-resolution measurement of collagen alignment in dynamically loaded soft tissue *J. Biomed. Opt.* **19** 066011
[269] Cronin T W *et al* 2003 Polarization signals in the marine environment *Polarization Science and Remote Sensing* (International Society for Optics and Photonics)
[270] Tyo J S, Goldstein D L, Chenault D B and Shaw J A 2006 Review of passive imaging polarimetry for remote sensing applications *Appl. Opt.* **45** 5453–69
[271] Tsai T-H and Brady D J 2013 Coded aperture snapshot spectral polarization imaging *Appl. Opt.* **52** 2153–61
[272] Tsai T-H, Llull P, Yuan X, Carin L and Brady D J 2015 Spectral-temporal compressive imaging *Opt. Lett.* **40** 4054–7
[273] Feng S *et al* 2019 Fringe pattern analysis using deep learning *Adv. Photon.* **1** 025001
[274] Miao X, Yuan X and Wilford P 2019 Deep learning for compressive spectral imaging *Digital Holography and Three-Dimensional Imaging 2019* (Bordeaux: Optical Society of America)
[275] Zhou C and Nayar S 2009 What are good apertures for defocus deblurring? *2009 IEEE Int. Conf. on Computational Photography (ICCP)* (Piscataway, NJ: IEEE)

Jinyang Liang is an Assistant Professor at the Institut National de la Recherche Scientifique (INRS) – Université du Québec. He directs the Laboratory of Applied Computational Imaging (LACI). His research interests cover ultrafast imaging, high-precision laser beam shaping, and photoacoustic microscopy. His research primarily focuses on implementing optical modulation techniques to develop new optical instruments for applications in physics and biology. He has published over 50 journal papers and conference proceedings. He has applied for seven patents on high-speed optical imaging technologies. He received the 2019–2022 Research Scholarship from FRQS, the 2019 Young Scientist Prize from IUPAP, the 2017 Educational Award – Gold from Edmund Optics, and the 2017 Discovery Accelerator Supplement Award from NSERC. He received his B.E. degree in Optoelectronic Engineering from Beijing Institute of Technology in 2007, and his M.S. and Ph.D. degrees in Electrical Engineering from the University of Texas at Austin, in 2009 and 2012. From 2012 to 2017, he was a postdoctoral trainee at Washington University in St. Louis and California Institute of Technology.